Wave overtopping at near-vertical seawalls

Influence of foreshore evolution during storms

Briganti, Riccardo; Musumeci, Rosaria Ester; van der Meer, Jentsje; Romano, Alessandro; Stancanelli, Laura Maria; Kudella, Matthias; Akbar, Rizki; Altomare, Corrado; Suzuki, Tomohiro; More Authors

DOI
10.1016/j.oceaneng.2022.112024

Publication date
2022

Document Version
Final published version

Published in
Ocean Engineering

Citation (APA)
Briganti, R., Musumeci, R. E., van der Meer, J., Romano, A., Stancanelli, L. M., Kudella, M., Akbar, R., Altomare, C., Suzuki, T., & More Authors (2022). Wave overtopping at near-vertical seawalls: Influence of foreshore evolution during storms. *Ocean Engineering*, *261*, Article 112024. https://doi.org/10.1016/j.oceaneng.2022.112024

Ocean Engineering 261 (2022) 112024

Contents lists available at ScienceDirect

Ocean Engineering

journal homepage: www.elsevier.com/locate/oceaneng

Wave overtopping at near-vertical seawalls: Influence of foreshore evolution during storms

Riccardo Briganti [a,*], Rosaria Ester Musumeci [b], Jentsje van der Meer [c,d], Alessandro Romano [e,f], Laura Maria Stancanelli [g], Matthias Kudella [h], Rizki Akbar [d], Ryard Mukhdiar [d], Corrado Altomare [i], Tomohiro Suzuki [j], Paolo De Girolamo [k], Giovanni Besio [l], Nicholas Dodd [m], Fangfang Zhu [n], Stefan Schimmels [h]

[a] Environmental Fluids Research Group, Faculty of Engineering, University of Nottingham, Nottingham NG7 2RD, UK
[b] Università degli Studi di Catania, Department of Civil Engineering and Architecture, Via Santa Sofia 64, 95123, Catania, Italy
[c] Van der Meer Consulting b.v., Ljouwerterdyk 55A, 8491ML, Akkrum, The Netherlands
[d] IHE Delft Institute for Water Education, PO Box 3015, 2601 DA Delft, The Netherlands
[e] Roma Tre University, Engineering Department, Via Vito Volterra, 62 - 00146, Rome, Italy
[f] IHCantabria - Instituto de Hidráulica Ambiental de La Universidad de Cantabria, Isabel Torres 15, 39011, Santander, Spain
[g] Department of Hydraulic Engineering, Delft University of Technology, Stevinweg 1, 2628 CN, Delft, The Netherlands
[h] Forschungszentrum Küste (FZK), Merkurstraße 11, D-30419, Hannover, Germany
[i] Maritime Engineering Laboratory, Universitat Politècnica de Catalunya - BarcelonaTech, Spain
[j] Flanders Hydraulics Research, Berchemlei 115, 2140 Antwerpen, Belgium
[k] Sapienza University of Rome, Department of Civil, Building and Environmental Engineering (DICEA), Via Eudossiana, 18 - 00184, Rome, Italy
[l] DICCA, Department of Civil, Chemical and Environmental Engineering, University of Genoa, Via Montallegro, 1, 16145, Genoa, Italy
[m] Faculty of Engineering, University of Nottingham, Nottingham NG7 2RD, UK
[n] Department of Civil Engineering, University of Nottingham Ningbo China, 199 Taikang East Road, Ningbo, 315100, China

ARTICLE INFO

Keywords:
Wave overtopping
Coastal flooding
Coastal structures
Storm sequences
Seawall
Beach foreshore

ABSTRACT

This work presents the results of an investigation on how wave overtopping at a near-vertical seawall at the back of a sandy foreshore is influenced by sequences of erosive storms. The experiments were carried out in the Large Wave Flume (GWK) at Leibniz University, Hannover (Germany). The tested layout consisted of a near-vertical 10/1 seawall and a sandy foreshore with an initial 1/15 slope. Three sequences of idealised erosive storms were simulated. Within each storm both the incident wave conditions and still water level were varied in time to represent high and low tide conditions. Each sequence started from a 1/15 configuration and the beach was not restored in between storms. The measurements included waves, beach profile, wave overtopping volumes. The profile of the beach was measured after each sea state tested.

Wave overtopping at each stage of the tested storms was significantly influenced by bed changes. This was linked to the measured evolution of the beach. Measurements showed that a barred profile developed quickly at the start of each sequence, and scour developed at the toe of the structure during high water level conditions, while accretion or partial backfilling developed during low water level conditions. Due to these processes, the position of a sea state in the tested sequence is shown to be an important factor in determining the wave overtopping volume. Remarkably, when a weaker idealised storm followed a more energetic one, nearly the same level of overtopping was recorded. This is explained by the foreshore erosion, leading to increased water depths and wave heights at the toe of the structure. This finding allows to quantify and to explain the variability of wave overtopping in storms following one another at intervals shorter than the recovery time of the foreshore.

1. Introduction

Coastal flood defence structures, in particular seawalls, are often found at the back of natural beaches. Erosive processes and scouring at the toe of the structures during storms can influence wave dissipation on their foreshore, and affect wave overtopping. This process is particularly important when storms arrive at intervals too short to allow

* Corresponding author.
E-mail address: riccardo.briganti@nottingham.ac.uk (R. Briganti).

https://doi.org/10.1016/j.oceaneng.2022.112024
Received 2 February 2022; Received in revised form 15 June 2022; Accepted 14 July 2022
Available online 12 August 2022

full beach recovery. Therefore, quantifying the influence of sequences of storms on seawalls performance, i.e., on wave overtopping, allows better modelling and design of coastal flood defences in presence of sandy foreshores.

Sequences of storms are documented and studied all over the world (e.g., Dissanayake et al., 2015a,b; Masselink et al., 2016; Besio et al., 2017; Eichentopf et al., 2020a; Baldock et al., 2021), and the focus of existing works is the understanding of the resulting cumulative erosion on natural beaches (Eichentopf et al., 2019; Sénéchal et al., 2017). On the other hand, the knowledge of the effects of storm sequences on engineered beaches (i.e., composite systems with a sandy foreshore and a backshore rigid wall), and in particular on the level of wave overtopping at a seawall, is much less developed. In general, investigations on wave overtopping considering the evolution of the foreshore profile are rare. As a matter of fact, only recently, laboratory experiments on the effect of the evolution of shingle beaches on wave overtopping at a seawall have been conducted (Salauddin and Pearson, 2019, 2020). Previous research showed that this type of structure induces lowering of the beach level in its proximity, due to scour at its toe (see Kraus and McDougal, 1996; McDougal et al., 1996, for a review). In turn, the foreshore morphology affects wave height and even spectral periods at the toe (Hofland et al., 2017). These two parameters significantly influence wave overtopping, as demonstrated experimentally (e,g, Altomare et al., 2016), therefore they are incorporated in the design formulae in EurOtop (2018). However, a detailed quantification of how a preceding storm affects the overtopping at a seawall due to the foreshore evolution has not yer been carried out. A strong motivation to investigate this process is that, during storm sequences, an enhancement of the impact of storms of moderate intensity in the erosion of natural beaches was documented (Lee et al., 1998; Splinter et al., 2014; Coco et al., 2014), while the potential analogous enhancement in wave overtopping has never been investigated in depth. Given the aforementioned occurrence of such sequences, this is a relevant gap in research.

The project ICODEP (Influence of foreshore evolution on COastal DEfence Performance), within the HYDRALAB-PLUS program, aims at quantifying the influence of foreshore profile evolution during sequences of storms on wave overtopping. To this end, a series of large-scale laboratory experiments were conducted on a flood defence made of a steep hard structure at the back of foreshore, representative of a seawall commonly found in coastal areas across the world. The incident wave conditions used were designed to simulate sequences of storms that did not allow recovery in between them. The experiments were carried out at the Large Wave Flume (GWK) at Leibniz University Hannover (Germany). A video sample of the experiments is available on the Hydralab+ YouTube channel.

Large flumes, such as the GWK and Delta Flume, were built to cope with morphodynamic scale effects and the possibility of their occurrence in wave overtopping in the presence of long foreshores were reported by Franco et al. (2009) and included in EurOtop (2007) and EurOtop (2018). Specific scaling relationships for flow and sediment transport variables are developed to assure that regimes are consistent in nature and in the model (Van Rijn et al., 2011; Frostick et al., 2011). Laboratory tests showed that large-scale setups are suitable to minimise scale effects in sediment transport (Van Rijn et al., 2011). Therefore, by using the GWK facility, it was possible to quantify the role of sequences of erosive storms and of evolving sandy beaches on overtopping processes at the seawall. Results of a comprehensive investigation on the main overtopping parameters, i.e., the number of overtopping events, overtopping volumes, discharges, and probability, are presented through the analysis of the ICODEP experimental results at storm and sequence scales.

This paper is organised as follows: after this introduction, the laboratory tests are described in detail in Section 2, then the results are presented and discussed in Section 3. Conclusions are presented in Section 4.

2. Laboratory tests

2.1. Experimental setup

The experimental layout (Fig. 1) consisted of a near vertical 10/1 sloped seawall and a sandy foreshore with an initial 1/15 slope. The natural sand of the beach had a nominal diameter (D_{50}) of 0.30 mm. The 1/15 slope for the foreshore was chosen for the present work as a benchmark slope, which had been extensively used in a number of previous experiments on sand beach evolution in the absence/presence of coastal structures/seawalls at GWK and other similar size facilities (e.g., Eichentopf et al., 2020b; Vousdoukas et al., 2014). The frame of reference used in this work had the origin of x at the neutral position of the wave paddle and the origin of z is set at the bottom of the flume. The y coordinate origin was located on the instrumented wall of the flume (see Fig. 2). The coordinates of the crest of the seawall were $x = 240.93$ m and $z = 5.5$ m. The toe of the beach is at $x = 161.9$ m. The model of the 10/1 battered (exposed with no toe revetment) wall (see Fig. 2) was made of a steel plate reinforced with plywood bars on the back and supported by a steel frame. This was anchored to the flume walls by two vertical rails. The structure toe at the beginning of each sequence was located at $x = 240.86$ m. Behind the steel seawall a vertical impermeable wall extended down to the bottom of the flume, in order to create a hydraulic disconnection for the groundwater flow between the beach and the sand at the back of the wall. The structure was buried in the sand for a depth of 0.9 m with respect to the initial level of the beach at the toe. Fig. 1 shows the positions of all the instruments along the foreshore, while Fig. 2 shows the seawall and all the instruments that are installed on it. A complete list of the coordinates of the instruments has been provided in a spreadsheet as additional material. A detailed description of the measurement equipment is given in Section 2.4

2.2. Test conditions

Three different sequences of wave and still water level (SWL) conditions were tested. Each sequence was made of 18 segments, each lasting $D_T = 32$ minutes, during which the SWL and wave parameters were varied. The segments were a combination of 3 groups of 6 waves and SWL combinations. These groups are referred here as storms because they were designed to be representative of idealised storm peaks and indicated as S1 and S2, corresponding to the two storm profiles defined, with S2 being the more energetic of the two. The six segments are referred to as T1 to T6. Waves were generated using the JONSWAP spectrum with a shape factor $\gamma = 3.3$; it is worth noticing that the significant distance travelled by the generated waves at uniform depth assured that these assumed intermediate water characteristics. Fig. 3 shows the time history of both the significant wave height (H_{m0}) and SWL conditions tested. The sequence of individual waves for each segment T was kept the same throughout the tests, in order to remove the variability due to the particular sequence of waves at the boundary (Romano et al., 2015, Williams et al., 2014, 2019). Two SWLs were applied during each storm; these were the same for storm S1 and S2. T3 and T4 were always tested with the SWL at 5.06 m from the bottom of the flume, and the rest of the storm was tested with the SWL at 4.60 m (see Table 2, 3, and 4 for details). As shown in Fig. 3, in both S1 and S2, H_{m0} increased from T1 to T2 at low SWL conditions, it reached a maximum at T3 in high SWL conditions and decayed afterwards from T4 to T6. The coincidence of maximum H_{m0} and maximum SWL was chosen because maximum overtopping is expected to occur when high tide and the maximum significant wave height occur at the same time. For example, this was the case of the storm on the east coast of England (U.K.) that occurred from 5th to 6th December 2013, when the peak storm H_{m0} coincided with high-water during spring-tide (Dissanayake et al., 2015b). To simplify the presentation of the results, unless individual segments are analysed, T3 and T4 will be

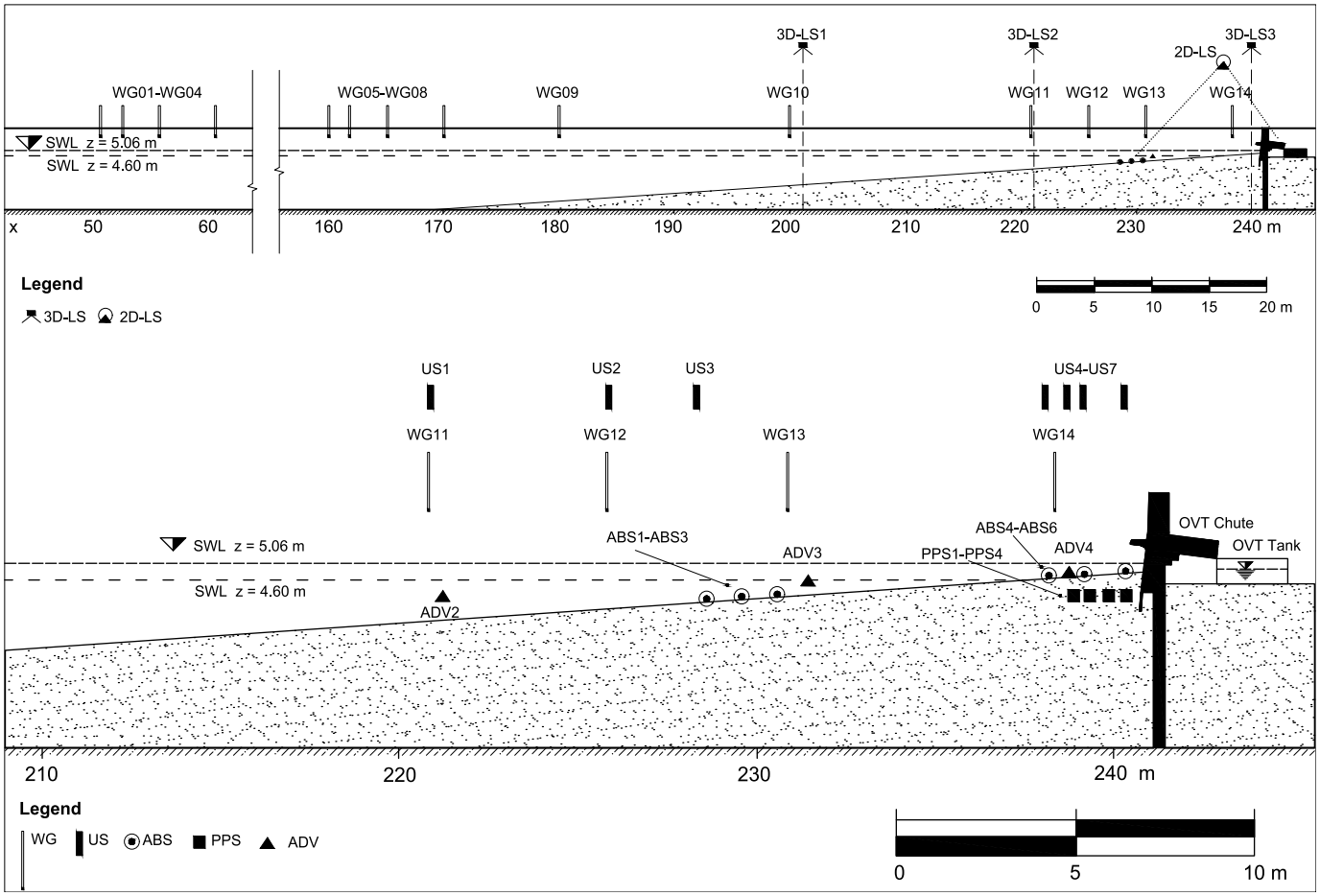

Fig. 1. Layout of the ICODEP seawall and foreshore, together with all the instruments installed. Upper panel: overview of the flume. Lower panel: close-up on the structure.

referred as peak conditions, T1 and T2 as pre-peak conditions, and T5 and T6 as post-peak conditions, for all storms.

S1 and S2 were combined into the three sequences C1-3 (see Table 1), each started from the 1/15 slope, while the beach profile after each storm was the initial one of the following storm. In C1 the repetition of the most energetic storm was tested, in order to measure the effects of previous bed evolution on the same storm. Conversely, C2 and C3 tested the effects of storms of different energy levels alternating. Note that no recovery occurred in between storms.

In this paper each sea state in a sequence is referred using the two characters codes in a sequence, separated by "-", in which first the sequence is indicated, then a number from 1 to 3 is used to identify the position of the storm in the sequence, followed by the codes for the storm and that of the sea state. For example, C3-2-S2-T4, indicates sea state T4 of the storm S2 that was second in the sequence C3.

Table 1
Storms order and initial bed conditions for the three sequences.

Sequence	Position	Storm profile	Initial beach profile
C1	1	S2	1/15 slope
	2	S2	As evolved due to previous S2
	3	S2	As evolved due to previous S2
C2	1	S2	1/15 slope
	2	S1	As evolved due to previous S2
	3	S2	As evolved due to previous S1
C3	1	S1	1/15 slope
	2	S2	As evolved due to previous S1
	3	S1	As evolved due to previous S2

2.3. Considerations on scale effects in the experiments

Although the ICODEP experiments are not meant to reproduce the aforementioned storms discussed in Dissanayake et al. (2015b), this reference case allows to estimate possible scale and model effects in the experiments. By using the maximum H_{m0} measured during the 5th December 2013 storm (storm D1 in Dissanayake et al., 2015b), to obtain the prototype H_{m0}, and the maximum H_{m0} of S2, to scale lengths in the model, we obtain the scaling factor for lengths $\lambda_H = H_{m0,pr}/H_{m0,m} = 6.25$, where the subscripts pr and m indicate prototype and model, respectively. The scaling factor for time (t) according to the Froude scaling laws ($\lambda_t = t_{pr}/t_m$) is $\lambda_t = \lambda_H^{0.5} = 2.5$. The focus of the experiment was on the peak of the storm, during which larger overtopping events are expected. The duration of each sea state ($D_T = 32$ min) was decided in order to generate a number of waves suitable to provide reliable estimates of wave overtopping, following Romano et al. (2015). This resulted in simulating about 8 hours at prototype scale for each individual storm. In the present work we aimed at analysing the performance of the seawall as flood protection. Therefore, in the laboratory, longer waves with respect to those in the field were generated, compatibly with the wave generation system of the facility. While in the 5th December 2013 storm, waves with steepness (estimated using the linear theory) $H_{m0}/gT_p^2 = O(0.006)$, where $g = 9.81$ m/s^2 is the acceleration of gravity and T_p is the peak period of the sea state, dissipated their energy through breaking on a unprotected sandy beach (D_{50} in the range 0.1 – 0.3 mm, slope about 1/66), in the laboratory $H_{m0}/gT_p^2 = O(0.004)$. Concerning the scaling of sediment transport processes, the correct scaling of the mobility

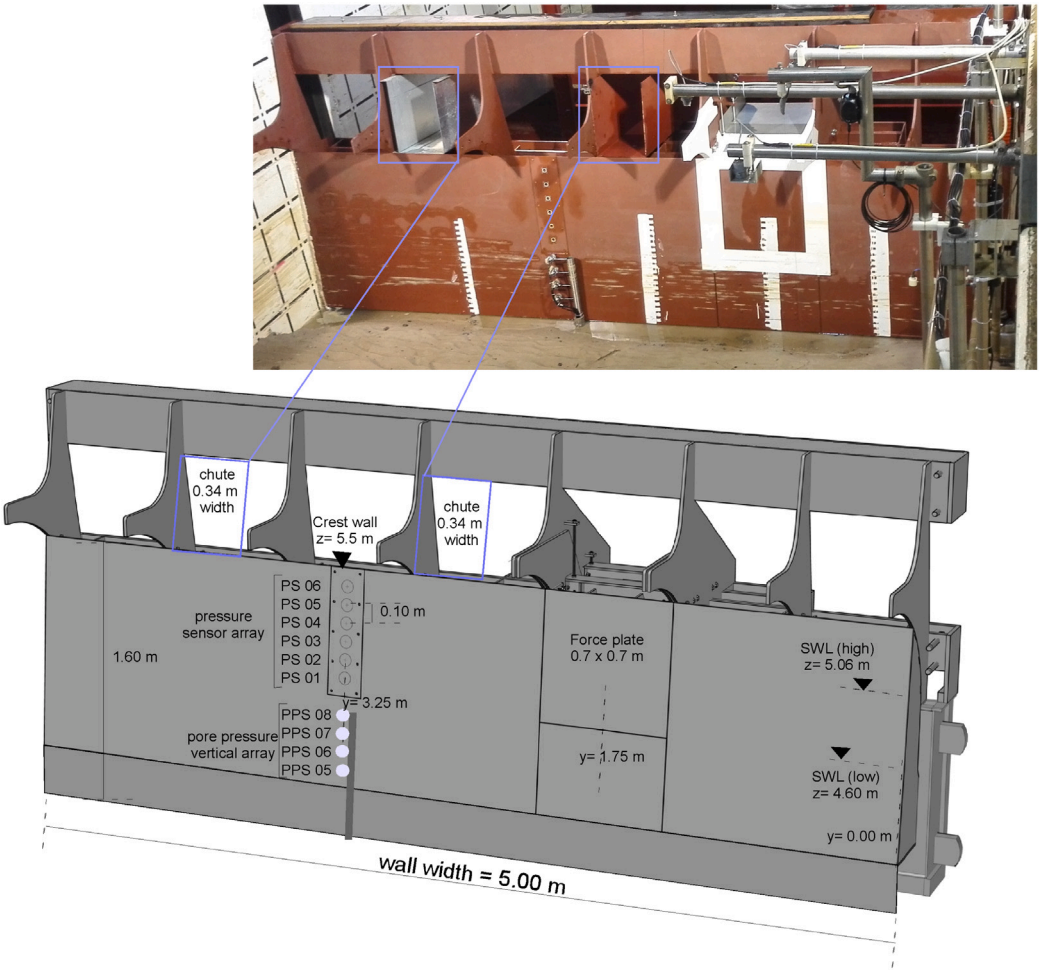

Fig. 2. Three-dimensional view of the tested seawall with the instruments installed.

parameter, which controls erosional processes, leads to the scaling factor for D_{50} is $\lambda_{D_{50}} = D_{50,pr}/D_{50,m} = \lambda_H \lambda_{f_b}$, where not only the geometrical scaling factor λ_H is considered, but also the scale of the bottom friction factor (f_b), i.e., $\lambda_{f_b} = f_{b,pr}/f_{b,m}$ (Van Rijn et al., 2011). When simulating storm conditions in the laboratory, as in the present case, the bedforms that develop are different from those in the prototype; in the field under stormy waves, usually, small scale bedforms, such as ripples, are not present, with $f_{b,pr} = O(0.01)$. On the contrary, these appear in the laboratory, leading to a much larger model friction factor: $f_{b,m} = O(0.05)$. As a result of these values, λ_{f_b} is generally smaller than 1 (Van Rijn et al., 2011). In the present case this leads to $\lambda_{D_{50}} = 1.25$ considering the indicative $\lambda_H = 6.25$. This behaviour is therefore favourable for modelling purposes, since it allows to the use of coarser model sediments, compared to the ones that would be obtained just considering the geometrical scale. In the present case, we have $D_{50,m} = 0.3$ mm. By applying $\lambda_{D_{50}} = 1.25$, $D_{50,pr} = 0.24$ mm, which means that the present results are valid for medium-fine sand.

2.4. Measurement equipment

2.4.1. Free surface measurements

The measurement of the free surface was carried out using 14 resistive wave gauges (WGs) and 7 ultrasonic wave gauges (USs). The positions of these instruments are shown in Fig. 1. An array of four WGs (WGs 01 to 04) was located at $x = 50.0$ m and it was used to compute the actual incident wave conditions using the Mansard and Funke (1980) method at the paddle. A second array of 4 WGs (WGs 05 to 08) was located at the toe of the beach starting from $x = 160$ m, WGs 05 to 07 were used to compute the actual incident wave conditions at the toe of the beach. The results of both arrays are shown in Tables 2, 3, and 4. Note that the nominal H_{m0} was always higher than the realised incident H_{m0} ($H_{m0,i}$). The reflection analysis shows that the incident spectral wave conditions did not change significantly on the horizontal portion of the flume, which was expected. Along the beach, WGs 08 to 14 were located in the shoaling and surf zones, while all seven USs were close to the structure. Note that US 1 and US 2 were co-located with WGs 10 and 11, respectively. It should be noted that WG 14 did not function properly during the experiments and it is not included in the analyses presented here.

An additional source of data for the free surface comes from one of the eight pore pressure sensors (PPSs) installed in the beach close to the toe of the structure. Four of these sensors (PPS 01 to 04) were installed along an horizontal array, always buried in the beach, while PPS 05 to 08 were located on a quasi-vertical array on the structure (see Fig. 2). These latter four sensors were unburied when erosion developed. In particular, it was observed in a series of preliminary tests that PPS 08 was exposed after just a few waves when erosion started.

2.4.2. Wave Overtopping measurements

A gravimetric overtopping tank with volume of 1.40 m^3 approximately was used to collect the overtopping water. The mechanism consisted of two tanks (inner and outer) and a connection to the crest of the wall by means of one or two chutes, depending on the SWL. The inner tank was placed on four force transducers (the positions of which are indicated in the additionally provided spreadsheet) that measured its weight during the tests. The outer tank provided a dry area around

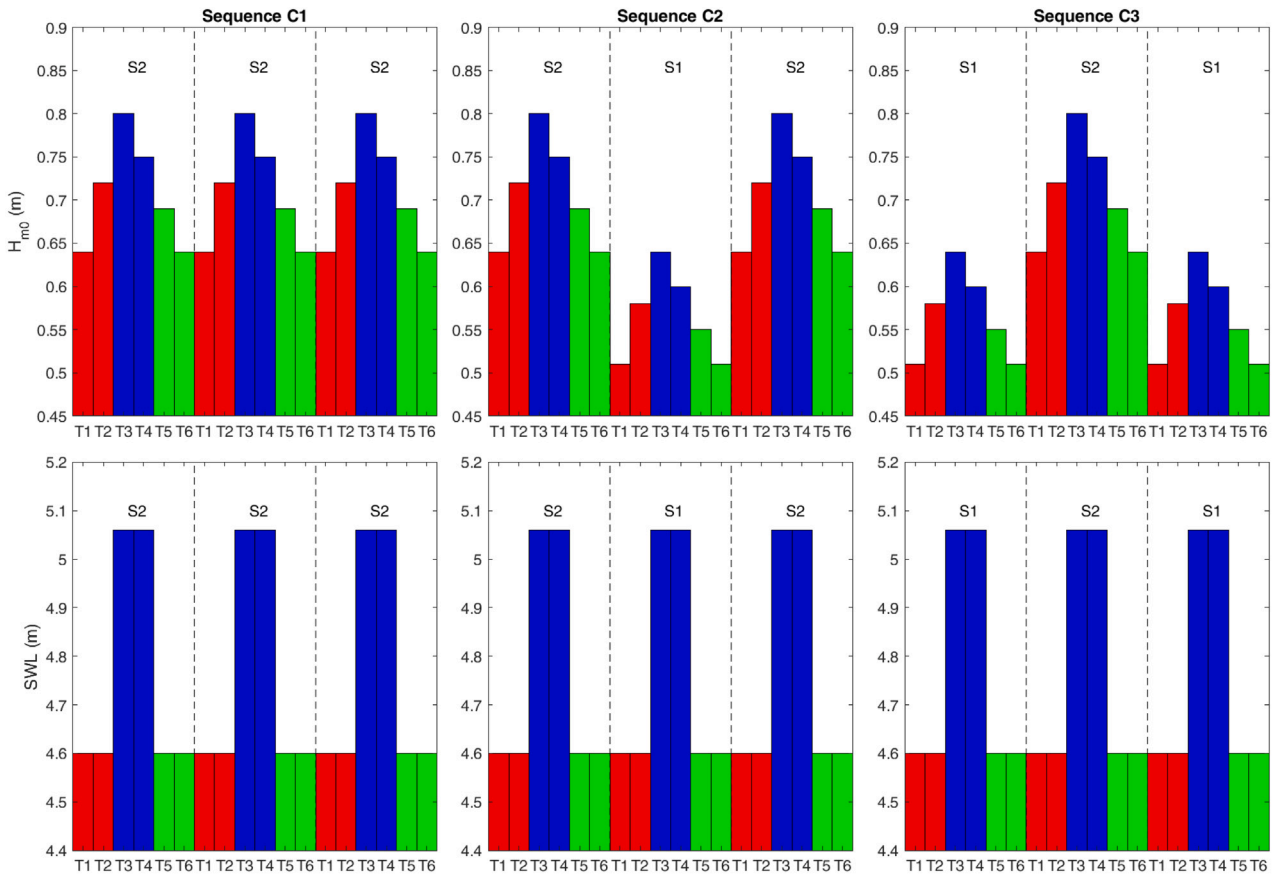

Fig. 3. Characteristics of the simulated storms. (For interpretation of the references to colour in this figure legend, the reader is referred to the web version of this article.)

Table 2
Target and incident wave conditions in sequence C1.

Test definition			Target at paddle		Actual at paddle		Actual at beach toe	
Test code	D_T (min)	SWL (m)	$H_{m0,i}$ (m)	T_p (s)	$H_{m0,i}$ (m)	T_p (s)	$H_{m0,i}$ (m)	T_p (s)
C1-1-S2-T1	32	4.6	0.64	3.9	0.61	4.00	0.61	4.00
C1-1-S2-T2	32	4.6	0.72	4.2	0.69	4.20	0.69	4.20
C1-1-S2-T3	32	5.06	0.8	4.5	0.77	4.43	0.77	4.55
C1-1-S2-T4	32	5.06	0.75	4.3	0.70	4.31	0.70	4.31
C1-1-S2-T5	32	4.6	0.69	4.1	0.66	4.20	0.66	4.20
C1-1-S2-T6	32	4.6	0.64	3.9	0.61	4.00	0.61	4.00
C1-2-S2-T1	32	4.6	0.64	3.9	0.61	4.00	0.61	4.00
C1-2-S2-T2	32	4.6	0.72	4.2	0.69	4.20	0.69	4.20
C1-2-S2-T3	32	5.06	0.8	4.5	0.78	4.43	0.78	4.43
C1-2-S2-T4	32	5.06	0.75	4.3	0.73	4.31	0.73	4.31
C1-2-S2-T5	32	4.6	0.69	4.1	0.66	4.00	0.66	4.00
C1-2-S2-T6	32	4.6	0.64	3.9	0.61	4.00	0.61	4.00
C1-3-S2-T1	32	4.6	0.64	3.9	0.62	4.00	0.62	4.00
C1-3-S2-T2	32	4.6	0.72	4.2	0.69	4.20	0.69	4.20
C1-3-S2-T3	32	5.06	0.8	4.5	0.79	4.43	0.79	4.43
C1-3-S2-T4	32	5.06	0.75	4.3	0.72	4.31	0.72	4.31
C1-3-S2-T5	32	4.6	0.69	4.1	0.66	4.20	0.66	4.00
C1-3-S2-T6	32	4.6	0.64	3.9	0.61	4.00	0.61	4.00

the inner tank to put the sensors. Also, a pumping system was used to pump away the collected water during the experiments. This was activated manually, with the trigger signal of the pump being recorded to identify the intervals of usage. The chute (0.34 m wide) was placed at the inner edge of the crest of the middle of the wall, connecting the structure and the inner tank. The number of chutes used depended on the water level. During low SWL conditions, two chutes were used, as opposed to high SWL ones, in which only one was used (with the only exception of C2-1-S2-T3 in which two chutes were used).

A pressure transducer (PS 07) was installed at the crest of the sloping wall, in the central chute, in order to make an estimation of the number of wave overtopping events. Furthermore, two synchronised video cameras recorded the overtopping events. The first camera was located at $x = 225.0$ m, at the level of the aisle along the flume, and the second one located close to the roof, at $x = 238.0$ m. Finally, in order to avoid problems due to the presence of the top beam of the structure, a plywood panel was installed on top of the beam that directed the entire overtopping volume within the chute.

2.4.3. Beach profile measurements

The beach profiles were obtained by a combination of data gathered by a mechanical wheel profiler, a Sick LMS291-S14 two-dimensional

Table 3
Target and incident wave conditions in sequence C2.

Test definition			Target at paddle		Actual at paddle		Actual at beach toe	
Test code	D_T (min)	SWL (m)	$H_{m0,i}$ (m)	T_p (s)	$H_{m0,i}$ (m)	T_p (s)	$H_{m0,i}$ (m)	T_p (s)
C2-1-S2-T1a	6	4.6	0.64	3.9	0.61	3.72	0.61	3.72
C2-1-S2-T1b	26	4.6	0.64	3.9	0.62	3.90	0.62	3.90
C2-1-S2-T2	32	4.6	0.72	4.2	0.69	4.20	0.69	4.20
C2-1-S2-T3	32	5.06	0.8	4.5	0.78	4.43	0.78	4.43
C2-1-S2-T4	32	5.06	0.75	4.3	0.73	4.31	0.73	4.31
C2-1-S2-T5	32	4.6	0.69	4.1	0.66	4.20	0.66	4.00
C2-1-S2-T6	32	4.6	0.64	3.9	0.61	4.00	0.61	4.00
C2-2-S1-T1	32	4.6	0.51	3.4	0.49	3.49	0.49	3.49
C2-2-S1-T2	16	4.6	0.58	3.7	0.55	3.56	0.55	3.56
C2-2-S1-T2	16	4.6	0.58	3.7	0.54	3.81	0.54	3.64
C2-2-S1-T3	16	5.06	0.64	3.9	0.64	4.00	0.64	3.81
C2-2-S1-T3	16	5.06	0.64	3.9	0.60	3.81	0.60	3.81
C2-2-S1-T4	32	5.06	0.6	3.7	0.58	3.64	0.58	3.72
C2-2-S1-T5	32	4.6	0.55	3.6	0.53	3.49	0.53	3.64
C2-2-S1-T6	32	4.6	0.51	3.4	0.48	3.28	0.48	3.41
C2-3-S2-T1	32	4.6	0.64	3.9	0.61	4.00	0.61	4.00
C2-3-S2-T2	32	4.6	0.72	4.2	0.69	4.20	0.69	4.20
C2-3-S2-T3	32	5.06	0.8	4.5	0.78	4.43	0.78	4.43
C2-3-S2-T4	32	5.06	0.75	4.3	0.73	4.31	0.73	4.31
C2-3-S2-T5	32	4.6	0.69	4.1	0.66	4.20	0.66	4.00
C2-3-S2-T6	32	4.6	0.64	3.9	0.61	4.00	0.61	4.00

Table 4
Target and incident wave conditions in sequence C3.

Test definition			Target at paddle		Actual at paddle		Actual at beach toe	
Test code	D_T (min)	SWL (m)	$H_{m0,i}$ (m)	T_p (s)	$H_{m0,i}$ (m)	T_p (s)	$H_{m0,i}$ (m)	T_p (s)
C3-1-S1-T1	32	4.6	0.51	3.4	0.49	3.49	0.49	3.49
C3-1-S1-T2	32	4.6	0.58	3.7	0.55	3.56	0.55	3.56
C3-1-S1-T3	32	5.06	0.64	3.9	0.62	4.00	0.62	3.81
C3-1-S1-T4	32	5.06	0.6	3.7	0.58	3.64	0.58	3.72
C3-1-S1-T5	32	4.6	0.55	3.6	0.53	3.49	0.53	3.64
C3-1-S1-T6	32	4.6	0.51	3.4	0.49	3.49	0.49	3.49
C3-2-S2-T1	32	4.6	0.64	3.9	0.61	4.00	0.61	4.00
C3-2-S2-T2	32	4.6	0.72	4.2	0.69	4.20	0.69	4.20
C3-2-S2-T3	32	5.06	0.8	4.5	0.78	4.43	0.78	4.43
C3-2-S2-T4	32	5.06	0.75	4.3	0.72	4.31	0.72	4.31
C3-2-S2-T5	32	4.6	0.69	4.1	0.66	4.20	0.66	4.00
C3-2-S2-T6	32	4.6	0.64	3.9	0.61	4.00	0.61	4.00
C3-3-S1-T1	32	4.6	0.51	3.4	0.49	3.49	0.49	3.34
C3-3-S1-T2	32	4.6	0.58	3.7	0.55	3.56	0.55	3.56
C3-3-S1-T3	32	5.06	0.64	3.9	0.62	3.81	0.62	3.81
C3-3-S1-T4	32	5.06	0.6	3.7	0.58	3.64	0.58	3.72
C3-3-S1-T5	32	4.6	0.55	3.6	0.53	3.49	0.53	3.64
C3-3-S1-T6	32	4.6	0.51	3.4	0.49	3.49	0.49	3.49

time of flight laser scanner (2D-LS hereinafter), and a Faro Focus 20/120 three-dimensional laser scanner (3D-LS hereinafter). The mechanical beach profiler was run to measure the initial planar slope and the profile after each test, from $x = 100.0$ m up to about $x = 240.3$ m, with a spatial resolution of $\Delta x = 0.25$ m. Point clouds of the bottom were obtained using the 3D-LS, which was moved at three measuring stations along the flume (see upper panel of Fig. 1). The resolution of the point clouds was $O(0.01$ mm). 3D reconstructions of the entire sandy bottom ($x > 190.0$ m) were obtained both at the beginning and at the end of each storm sequence, when the flume was drained before beach reshaping. Additional 3D-LS measurements of the region close to the wall, 231.5 m $< x < 241.0$ m, were obtained in dry conditions in the upper part of the beach. In particular, the beach profile was extracted from the 3D point cloud by spanwise averaging the points gathered along a central stripe, 2.49 m $< y < 2.51$ m. 2D-LS measurements running continuously during each test provided information on the foreshore evolution in proximity of the wall. Its measuring range was 228.5 m $< x < 243.5$ m. Due to physical constraints, the mechanical wheel profiler could not reach the toe of the wall, located at about $x = 240.9$ m. The data on the near-wall bed profile obtained by the 3D scanner, for the initial condition and at the end of sea states T2, T4 and T6 were used to complete the beach profile for the last 60 cm. For sea states T1 and T5 the data of the 2D-LS were used for the same purpose. Due to the presence of water, it was not possible to have data on the bottom morphology at the toe of the wall at the end of all the sea states T3, in high SWL conditions, and for some of the T5 sea states, as the scour was flooded notwithstanding the fact that the SWL was lowered. The complete beach profiles were then obtained by joining the offshore part of the wheel profiler data and onshore part of the 3D/2D scanners data. More details on the profiles data processing can be found in Mukhdiar (2017). Finally, the scour evolution was also monitored by the same video camera used for wave overtopping. To this end, four rulers were attached to the sloping wall, in order to have a visual reference of the scour depth.

2.4.4. Other instruments

Other sets of instruments were installed to measure forces and pressures on the wall, sediment transport, and flow velocity in the surf zone and close to the wall. Since the focus of this paper is wave overtopping, these are only mentioned here and shown in Fig. 2 for completeness, the reader is referred to Briganti et al. (2018) for more details. In order to measure pressures on the wall, an array of six PSs (1 to 6) was installed and forces were measured on the wall using a plate at which 5 load cells were connected. Additionally, sediment transport

was measured by two Acoustic Backscattering Sensors (ABS), and four Acoustic Doppler Velocimeters (ADVs) were used to measure local flow velocity, these were located along the whole active part of the beach.

3. Results and discussion

3.1. Foreshore evolution

The foreshore evolution is studied by analysing the bed change after each segment T with respect to the initial bed profile $\Delta z_b = z_b(t_{e,s}) - z_b(t_0)$, where z_b is the bed level from the bottom of the flume, $(t_{e,s})$ is the end time of each sea state $(s = 1, 2, \ldots, 6)$ and t_0 is the start time of each sequence, when the beach had its 1/15 slope. The intra-storm evolution of the bed is qualitatively similar in all cases. Fig. 4 shows Δz_b for the first storm of C1 (namely C1-1-S2) as an example. At the start of the sequence, during T1, a bar started developing and grew in the subsequent sea states. At the same time erosion developed in the region between the bar and the wall, approximatively between $x = 230.0$ m and $x = 240.86$ m. The evolution close to the structure is more complex as accretion occurred during the first storm of the sequence. During T2 the bar grew and migrated offshore, while the erosion of the region between the bar and the structure increased.

During peak conditions significant erosion developed near the toe of the structure. Also, it appears that partial backfilling occurred and Δz_b reached almost zero around $x = 236.0$ m during T4. The backfilling in this region reversed to erosion in the subsequent T5, while partial filling of the scour at the toe of the seawall and continued in T6.

The second storm of the sequence (C1-2-S2) started from a barred beach configuration. The bar continued to grow, as shown in Fig. 5. Δz_b is negative overall close to the structure. However, during peak conditions, the evolution of the region between the bar and the seawall is more complex, with deposition occurring just offshore the scour area.

Fig. 6 shows the initial and final profile for the three sequences together with the range of z_b reached. Results are consistent across all three sequences and the evolution of the beach is described by dividing it into four zones. Zone 1 is the ripple region extending approximatively from $x = 200.0$ m to $x = 217.0$ m. Zone 2 is the bar region extending approximatively from $x = 217.0$ m to $x = 230.0$ m in C1 and C3; here the bar formed and migrated offshore during each sequence. The boundary between Zone 2 and 3 is a pivot around which the beach rotated. Zone 3 is characterised by overall erosion with respect to the initial profile, as the figure shows. However, in Zone 3 backfilling occurred at high SWL conditions as shown in Fig. 5; this could be large enough to establish a secondary bar above the original profile as the results for C1 (panel *a* of Fig. 6) show. The slope of Zone 3 was milder than the original 1/15 and appeared to be almost zero in the upper part of this region in all sequences. This "terrace" formed at the position of the initial shoreline at the lower SWL. This is considered as the boundary with Zone 4. Here both swash motion and scour had an important role in modelling the beach.

3.2. Spatial and time wave height evolution

The total (incident plus reflected) H_{m0} along the flume was computed using the signals recorded by the resistive and the acoustic wave gauges when available. Because of the intense wave breaking, and consequent presence of two-phase flow, spikes due to bubbles and spray were present. These were removed using the procedure proposed by Mori et al. (2007), originally developed for ADVs. However, even after de-spiking, the signal was still corrupted in some time series. These data were disregarded. As a result of this preliminary data vetting, only a few time series from the acoustic wave gauges are available for the T3 and T4 sea states, while the coverage of pre- and post-peak conditions is much more consistent. In peak conditions the signal from PPS 8 ($x = 240.84$ m $z = 4.805$ m) was used to obtain the time series of the free surface. The vertical array of PPSs from 5 to 8 was initially buried at the beginning of the sequence but was rapidly uncovered during erosive conditions. In particular, PPS 08 was rapidly exposed after a few waves, hence it was used for obtaining information on the waves near the toe of the structure without considering the attenuation of the soil. Since the elevation of PPS 08 from the bed level during the test is unknown, and shallow water conditions are met at the toe of the structure, the hydrostatic assumption is used to provide the position of the free surface from the pressure signal using the well known relationship: $\eta = \Delta p/(\rho g)$, where Δp is the differential pressure measurement, $\rho = 1000$ kg/m^3 is the water density.

The low frequency portion of the wave energy density spectrum during the experiments has an important role in wave overtopping, therefore it is studied here. The low frequency waves in the experiments comprise bound incident waves, free low-frequency wave reflected by the beach, and free long waves reflected at the paddle and not fully absorbed by the active absorption system. All these contributions are not untangled here, and the same procedure as in Romano et al. (2015) is followed to separate the low frequency waves as a whole from the total recorded spectrum. The significant wave height was computed for the range of frequencies lower than those of the JONSWAP spectrum generated, i.e., for spectral components lower than a threshold value for the frequency f. By analysing the generated spectra the value $f = 0.15$ Hz was determined for the separation. The significant wave height computed for $f < 0.15$ Hz is referred to as $H_{m0,low}$. It is determined from WGs in pre- and post-peak conditions and using PPS 08 in peak ones. The significant wave height computed from the whole signal is simply referred as H_{m0} (from WGs and USs in pre-post peak conditions and from PPS 08 in peak ones).

Note that the co-located USs and WGs give slightly different H_{m0}, with the acoustic sensors providing slightly higher values. A typical evolution of H_{m0} during the six segments of a storm is shown in Fig. 7 for storm C1-1-S2. The figure shows that for pre- and post-peak conditions waves break on the bar and H_{m0} decays up to the structure toe. In these conditions low-frequency waves are energetic in the region between the bar and the structure, particularly close to the wall, and they are the dominant drivers in the inner surf zone as shown by US 6 and 7 ($x = 239.28$ m $x = 240.38$ m respectively) in Figs. 8 and 9.

For the peak conditions, wave breaking and wave reflection dominate wave propagation. H_{m0} decays on the bar, as shown by WG 12 ($x = 225.88$ m) and 13 ($x = 230.88$ m) in Figs. 8 and 9. However, waves retain a significant amount of energy at the structure toe (e.g., $H_{m0,p} = 0.5$ m in C1-1-S2-T3). The initial bed configuration influences H_{m0} along the beach, in both high and low SWL conditions. Examples of the latter cases are shown in Figs. 8 and Fig. 9; these figures show the variation of H_{m0} along the beach for T1 for S1 and S2 when the storms start from 1/15 slope and from barred beach configurations. The development of the bar shifts the onset of breaking offshore; at the same time the inshore erosion and flattening of the beach generates an increase of the H_{m0} close to the structure. These two simultaneous processes are quantified in Fig. 10 for all the low SWL sea states. Here H_{m0} and $H_{m0,low}$ at the bar and the toe of the structure for the same storm at different positions in the sequence are shown. The signal at WG 12 is used for computing the significant wave height at the bar, while all the valid measurements at US 6 and PPS 8 are used to quantify H_{m0} and $H_{m0,low}$ at the toe of the structure. The bar attenuates H_{m0} at WG 12 with respect to the plane slope configuration, as shown in Fig. 10 (panel *a*). This effect is more pronounced in pre-, than in post-peak conditions. $H_{m0,low}$ is affected by the initial beach configuration only in peak conditions, as shown in panel *b* of Fig. 10. At the toe of the structure there is an increase of H_{m0} and $H_{m0,low}$ for most of the storms (Fig. 10, panels *c*, *d*). This is the effect of the erosion in Zones 3 and 4. Only in one case H_{m0} is lower for the second storm than that of the first. This is because, for this particular sea state, the erosion close to the structure is small, hence the dissipation on the bar is effective in reducing the wave height. As shown in the comparison between panel *c* and *d* of Fig. 10, in pre- and post-peak conditions $H_{m0,low}$ and H_{m0} have nearly the same value, indicating that low frequencies dominate wave conditions at the toe and, in turn, wave overtopping at the seawall.

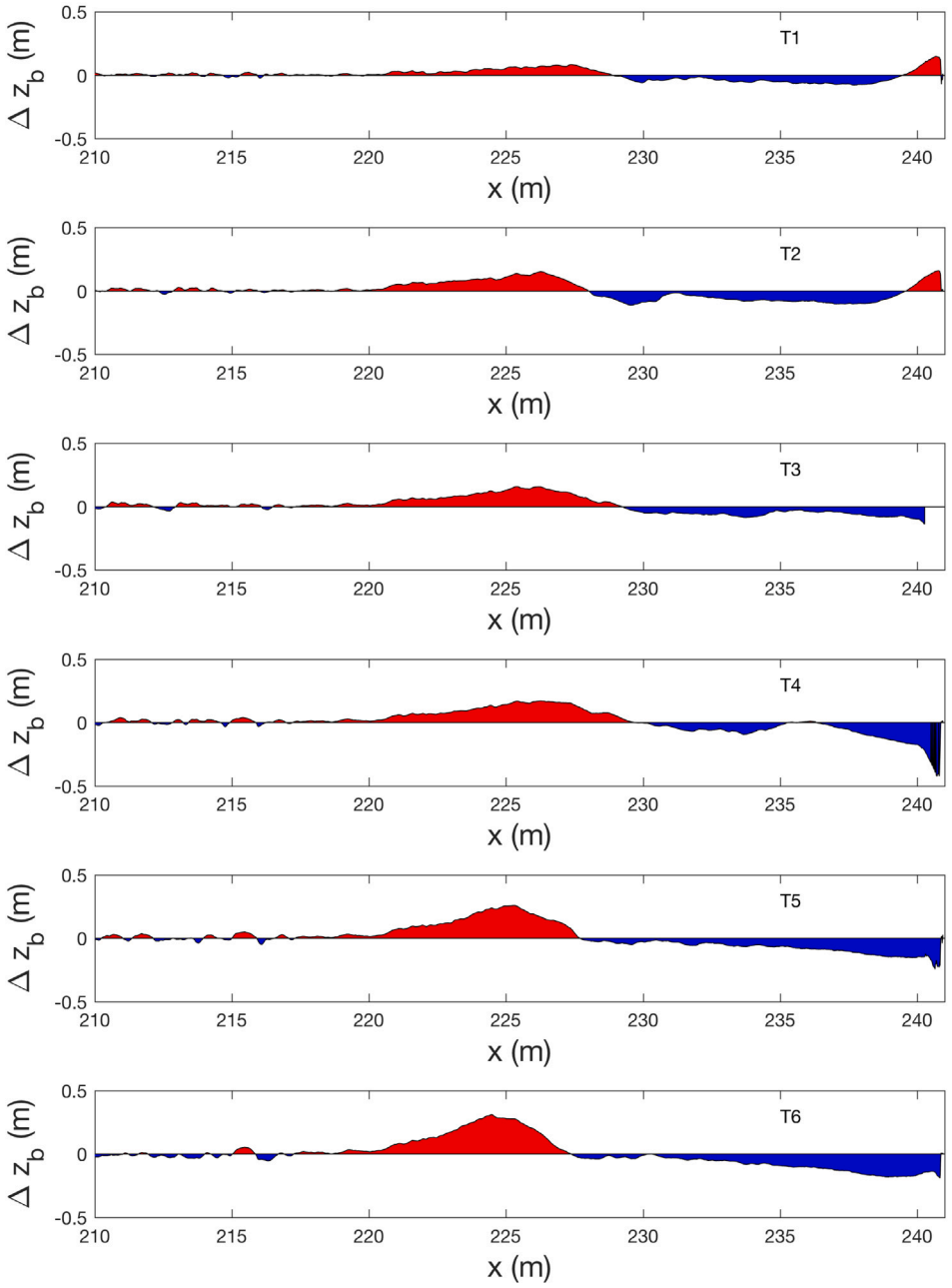

Fig. 4. Δz_b for each sea state of the storm C1-1-S2. From top to bottom: segment T1 to segment T6. Red: accretion, blue: erosion. (For interpretation of the references to colour in this figure legend, the reader is referred to the web version of this article.)

3.3. Wave Overtopping

3.3.1. Overtopping parameters computation

The weight of the water collected by the chutes into the tank was recorded by four load cells during each test. The sum of the measurement by each load cell gave the total weight of overtopping water. The instantaneous volume of water is obtained by dividing the weight by ρg. The data were smoothed using a moving average filter with a window size equal to the nominal wave peak period T_p of each experiment. The pumping system in the overtopping tank was not activated during low SWL conditions when only a few waves were overtopping. Conversely, the pump was manually activated to avoid overfilling of the overtopping tank during high SWL conditions. An example of wave overtopping data for a high SWL condition is shown in Fig. 11. Note that the trigger function is defined between 0 and 1, and the square waves identify the intervals during which the pump was activated, although in the raw signal oscillations around 0 occured when the pump was not active. As seen in the figure, almost all waves were overtopping and it was necessary to activate the pump multiple times in these conditions (typically 3 to 5 times per sea state). The pump discharge was calibrated in a dedicated set of tests.

The mean overtopping discharge for each segment q is computed following the methodology shown in Appendix. Note that here, only results using Eq. (A.2) are shown.

The number of overtopping events for each segment (N_{ov}) is an important parameter in assessing overtopping. This was evaluated using the pressure transducer installed in the chute PS 7, in conjunction with the overtopping tank measurements and the video cameras records. The ratio between N_{ov} and the number of incident waves obtained by zero-crossing analysis of the incident wave time series calculated using WG $1-4$ is the percentage of overtopping (P_{ov}). Other authors (e.g. Chen et al., 2016) use the incident time series at the toe of the structure.

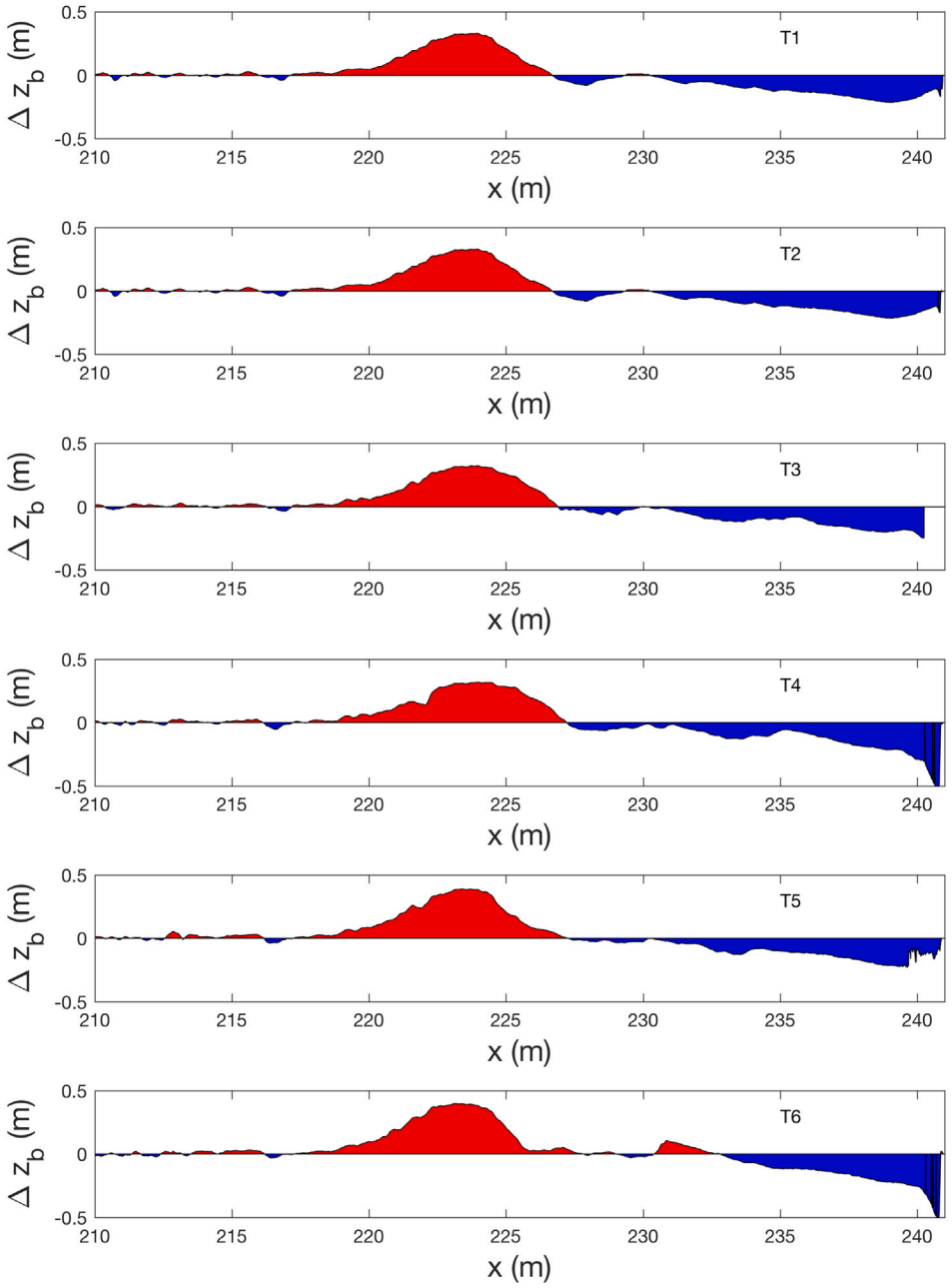

Fig. 5. Δz_b for each sea state of the storm C1-2-S2. From top to bottom: segment T1 to segment T6. Red: accretion, blue: erosion. (For interpretation of the references to colour in this figure legend, the reader is referred to the web version of this article.)

However, in this case, intense wave breaking on the foreshore makes the computation of the incident time series with the traditional three gauges waves not accurate. Alternatively numerical methods could be used, but this is beyond the scope of the present paper. Tables 5, 6, 7 show q, N_{ov} and P_{ov} for all sea states tested in sequence C1, C2, and C3 respectively. The individual overtopping volumes data from the measurement is used for further analysis of the overtopping volume distribution. To this end, the time series of overtopping volumes in the tank, together with the overtopping events record from PS 07, were used. The computation was carried out only when the pumps were not activated to avoid inaccuracy due to the presence of the outgoing flow. Only peak conditions were considered. Fig. 13 shows the example of the procedure used for determining the individual overtopping volumes. More details on the overtopping data processing can be found in Akbar (2017).

3.3.2. Overtopping rates

Fig. 12 shows q for the three sequences of storms; pre-peak, peak, and post-peak conditions are highlighted in different colours. Note that, for pre- and post-peak conditions overtopping is always caused by only a few waves and it is always three orders of magnitude lower than peak conditions. The first T1 for each sequence, i.e., that with a 1/15 slope as initial configuration, has always no measurable overtopping. In subsequent storms of the sequences, T1 shows some overtopping, for both S1 and S2. In C1, in which S2 is repeated three times, for pre-peak conditions, q increases with the position within the sequence. These results show that q varies significantly with the initial configuration of the beach for a given set of hydrodynamic forcing in low SWL. For example in C1-1-S2-T1 no wave was overtopping, while in C1-3-S2-T1 it was measured $q = 0.024$ l/s/m and $P_{ov} = 4.54\%$. Similar considerations apply to the post peak results for q (in green in Fig. 12). The variability of q with the initial conditions for the beach is better

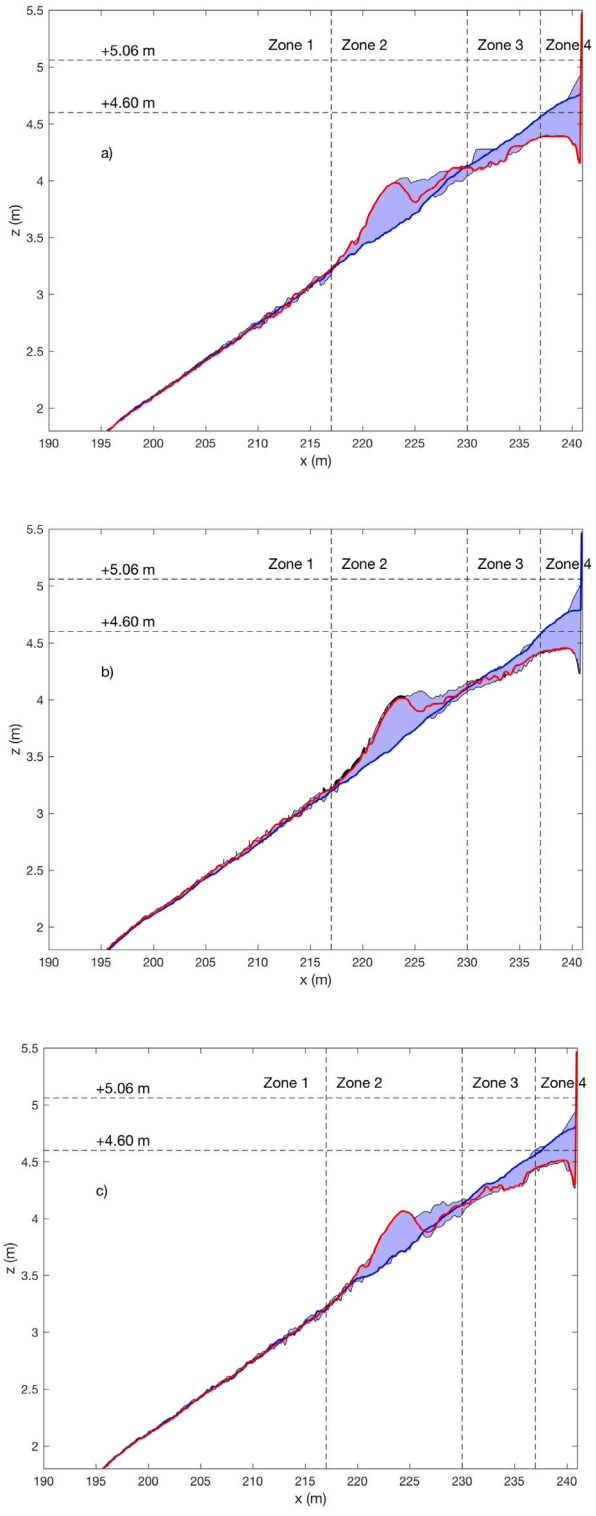

Fig. 6. Zones of the beach evolution for sequence. Blue line: initial profile, red line: end profile. The blue shaded area is the range of the bed level at each position. (*a*) C1 (*b*) C2, (*c*) C3. (For interpretation of the references to colour in this figure legend, the reader is referred to the web version of this article.)

shown in peak conditions (in blue in Fig. 12). In sequence C1, there is a slight monotonic increase in q within the whole sequence. More importantly, in C2, the peak of the second storm (S1), although of lower energy, shows nearly the same q as the previous S2. If compared with the results of storm S1 as first of sequence C3, the peak of storm S1 as second storm of sequence C2 shows a much higher q. For C2-2-S1-T3 $q = 8.45$ l/s/m compared to $q = 5.31$ l/s/m for C3-1-S1-T3. Consistently, in C3, q for storm S1 as third storm in the sequence, nearly doubles with respect to q for storm S1 as first.

The cumulative overtopping volume per unit width for each storm (V_{tot}) is computed in time over the six segments of 32 min that form each S. This parameter indicates the cumulative overtopping for a

Table 5
Wave overtopping parameters q, N_{ov}, and P_{ov} for sequence C1.

Test code	q (l/s/m)	N_{ov} (–)	P_{ov} (%)
C1-1-S2-T1	0.000	0	0
C1-1-S2-T2	0.009	4	0.85
C1-1-S2-T3	9.47	380	84.82
C1-1-S2-T4	7.86	426	89.68
C1-1-S2-T5	0.008	14	2.86
C1-1-S2-T6	0.004	8	1.59
C1-2-S2-T1	0.001	7	1.38
C1-2-S2-T2	0.009	13	2.78
C1-2-S2-T3	11.33	410	92.76
C1-2-S2-T4	9.86	418	87.63
C1-2-S2-T5	0.019	28	5.70
C1-2-S2-T6	0.009	21	4.13
C1-3-S2-T1	0.006	23	4.54
C1-3-S2-T2	0.024	39	8.16
C1-3-S2-T3	11.84	397	89.41
C1-3-S2-T4	11.30	419	87.29
C1-3-S2-T5	0.020	45	9.15
C1-3-S2-T6	0.009	30	5.86

Table 6
Wave overtopping parameters q, N_{ov}, and P_{ov} for sequence C2.

Test code	q (l/s/m)	N_{ov} (–)	P_{ov} (%)
C2-1-S2-T1 (a+b)	0.000	0	0.00
C2-1-S2-T2	0.011	4	0.85
C2-1-S2-T3	9.47	420	93.96
C2-1-S2-T4	7.86	430	90.34
C2-1-S2-T5	0.002	11	2.24
C2-1-S2-T6	0.003	8	1.60
C2-2-S1-T1	0.002	1	0.17
C2-2-S1-T2	0.003	3	0.56
C2-2-S1-T3	8.45	451	89.13
C2-2-S1-T4	6.36	442	80.51
C2-2-S1-T5	0.006	5	0.89
C2-2-S1-T6	0.001	3	0.52
C2-3-S2-T1	0.006	10	1.97
C2-3-S2-T2	0.011	13	2.75
C2-3-S2-T3	11.23	415	93.89
C2-3-S2-T4	8.93	438	91.63
C2-3-S2-T5	0.013	18	3.66
C2-3-S2-T6	0.007	13	2.54

Table 7
Wave overtopping parameters q, N_{ov}, and P_{ov} for sequence C3.

Test code	q (l/s/m)	N_{ov} (–)	P_{ov} (%)
C3-1-S1-T1	0.000	0	0
C3-1-S1-T2	0.002	1	0.18
C3-1-S1-T3	5.31	442	87.35
C3-1-S1-T4	3.97	464	85.14
C3-1-S1-T5	0.001	3	0.54
C3-1-S1-T6	0.000	0	0
C3-2-S2-T1	0.002	3	0.59
C3-2-S2-T2	0.007	7	1.49
C3-2-S2-T3	10.40	423	94.84
C3-2-S2-T4	9.31	440	93.02
C3-2-S2-T5	0.008	16	3.27
C3-2-S2-T6	0.003	6	1.19
C3-3-S1-T1	0.003	5	0.85
C3-3-S1-T2	0.005	8	1.47
C3-3-S1-T3	10.31	464	91.34
C3-3-S1-T4	8.64	461	83.97
C3-3-S1-T5	0.001	5	0.89
C3-3-S1-T6	0.001	2	0.34

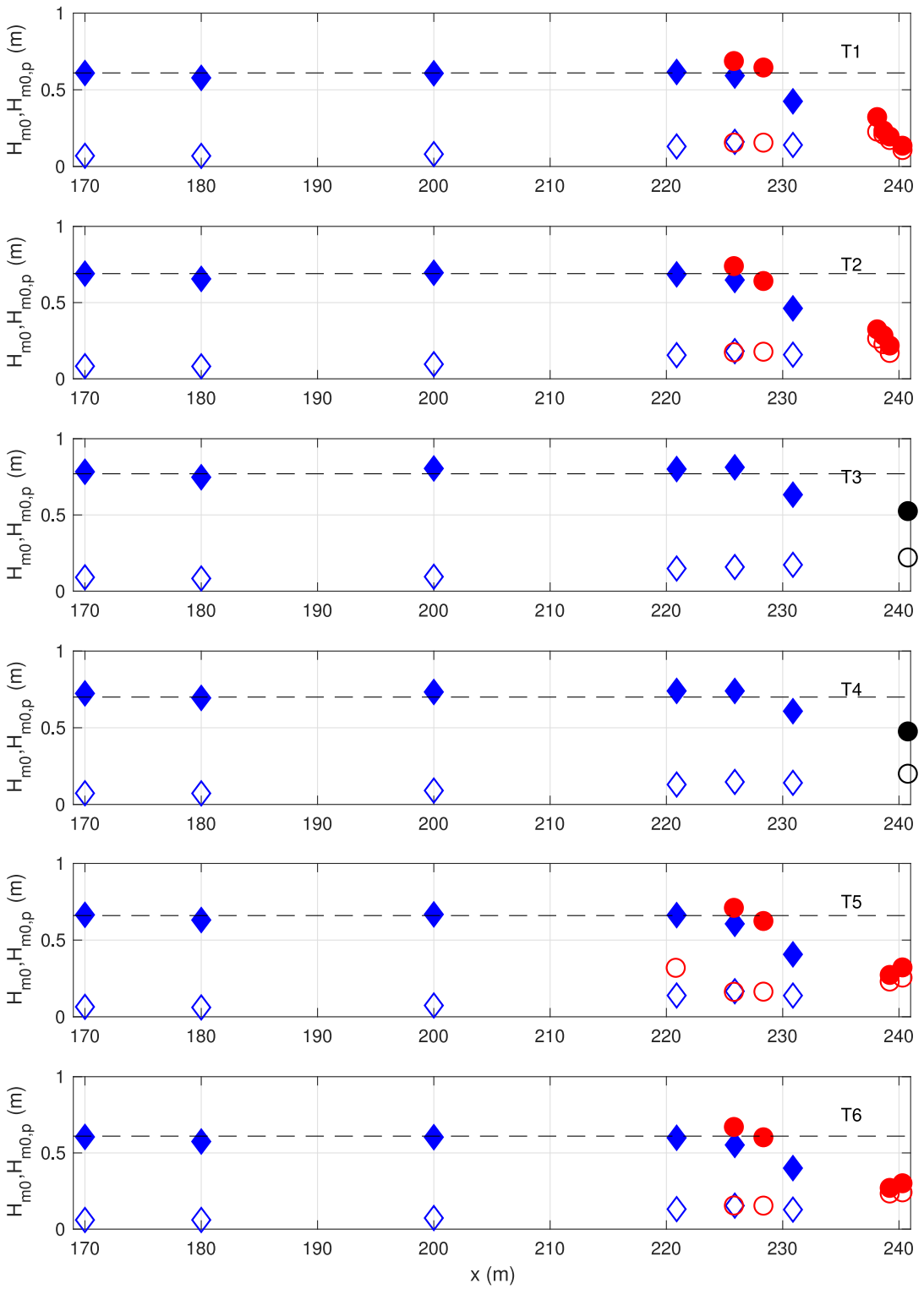

Fig. 7. Evolution of H_{m0} and $H_{m0,p}$ during the storm C1-1-S2 in all six sea states. From top to bottom: segment T1 to segment T6. Solid markers: total H_{m0} and $H_{m0,p}$. Blank markers: $H_{m0,low}$. Blue diamonds: measurements from WGs, red circles: measurements from US, black circles: measurements from PPS 8. (For interpretation of the references to colour in this figure legend, the reader is referred to the web version of this article.)

storm, therefore, by comparing V_{tot} for the same storm type at different positions in a sequence, i.e., for the same forcings, but different initial beach profile, it is possible to quantify the effect of the initial foreshore configuration on wave overtopping. For this purpose we define $V_{tot,i}$ ($i = 1, 2, 3$) to distinguish V_{tot} computed for the i-th storm of a sequence (e.g., $V_{tot,2}$ indicates V_{tot} of the second storm in the sequence). Note that C1-1-S2 is used as reference for S2 for $V_{tot,1}$. Fig. 14 shows a comparison between V_{tot} for a storm type tested as first in the sequence ($V_{tot,1}$) with V_{tot} for the same storm either second or third in a sequence. V_{tot} increases in all cases for both storms starting at least second in

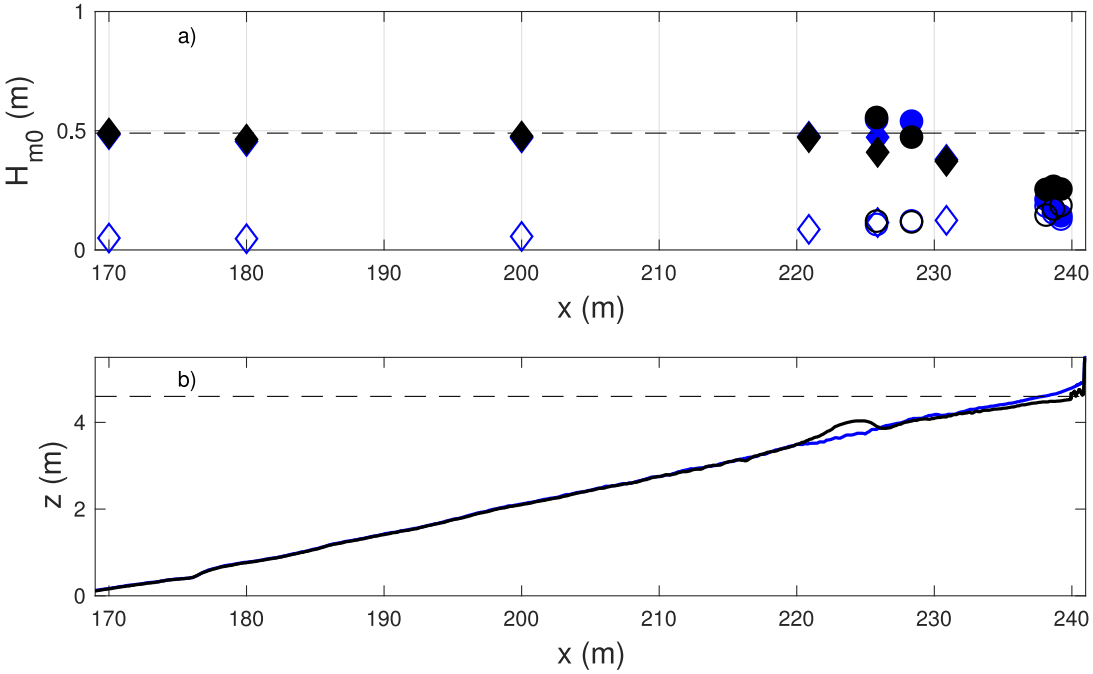

Fig. 8. (*a*) Comparison of H_{m0} during the sea state T1 for the storm C3-1-S1 (blue markers) and C3-3-S1 (black markers). Diamonds: *WGs*, circles *USs*. Solid markers: total H_{m0}. Blank markers: $H_{m0,low}$. (*b*) Bottom profile, blue: at the end of C3-1-S1-T1, black: C3-3-S1-T1. (For interpretation of the references to colour in this figure legend, the reader is referred to the web version of this article.)

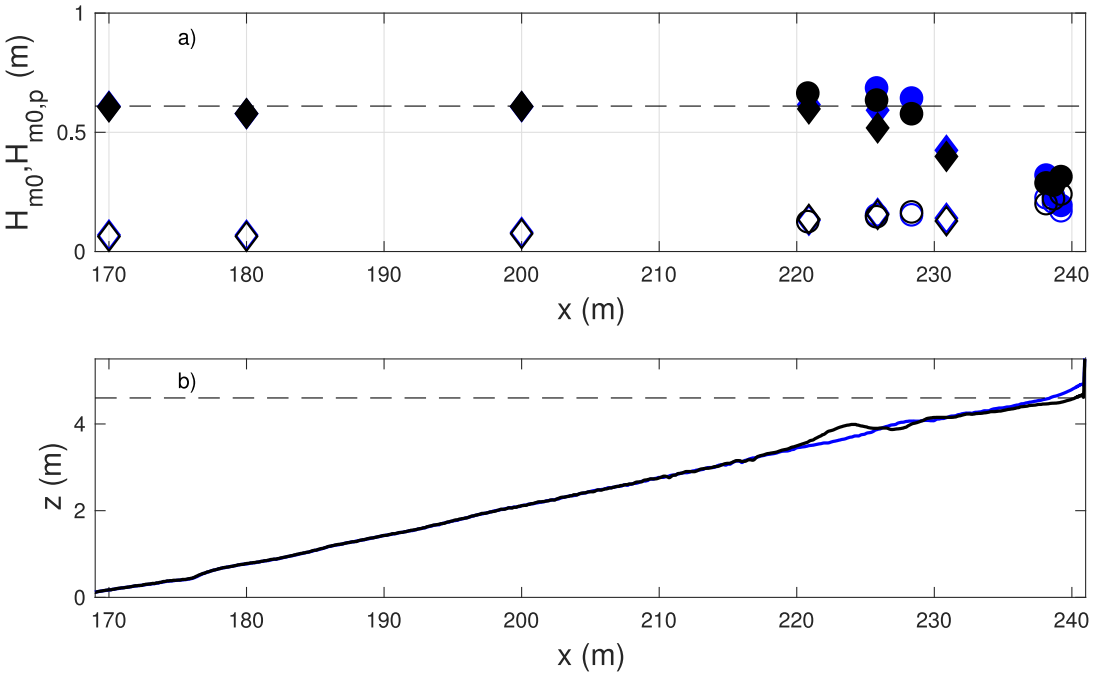

Fig. 9. (*a*) Comparison of H_{m0} and $H_{m0,p}$ during the sea state T1 for the storm C1-1-S2 (blue markers) and C1-2-S2 (black markers). Diamonds: WGs, circles USs. Solid markers: total H_{m0}. Blank markers: $H_{m0,low}$. (*b*) Bottom profile, blue: at the end of C1-1-S2-T1, black: C1-2-S2-T1. (For interpretation of the references to colour in this figure legend, the reader is referred to the web version of this article.)

the sequence. However, differences between storms S1 and S2 are noteworthy. We introduce $\delta V_{tot} = \frac{V_{tot,j} - V_{tot,1}}{V_{tot,1}} \times 100$, where $j = 2, 3$. δV_{tot} is the percentage variation of V_{tot} for the same storm between the value at second or third position in the sequence ($V_{tot,2}$ and $V_{tot,3}$ respectively) and $V_{tot,1}$, normalised with $V_{tot,1}$. δV_{tot} is higher for the weaker storm tested than for the more energetic one. In fact, for storm C2-2-S1, $V_{tot,2}$ is 59% higher than that of C3-1-S1, while for C3-3-S1, $V_{tot,3}$ increases by 104%. For S2; δV_{tot} ranges between

3.4. Statistical distribution of overtopping volumes

The distribution of the individual overtopping volumes is studied here for the peak sea states (T3 and T4). The Weibull distribution is

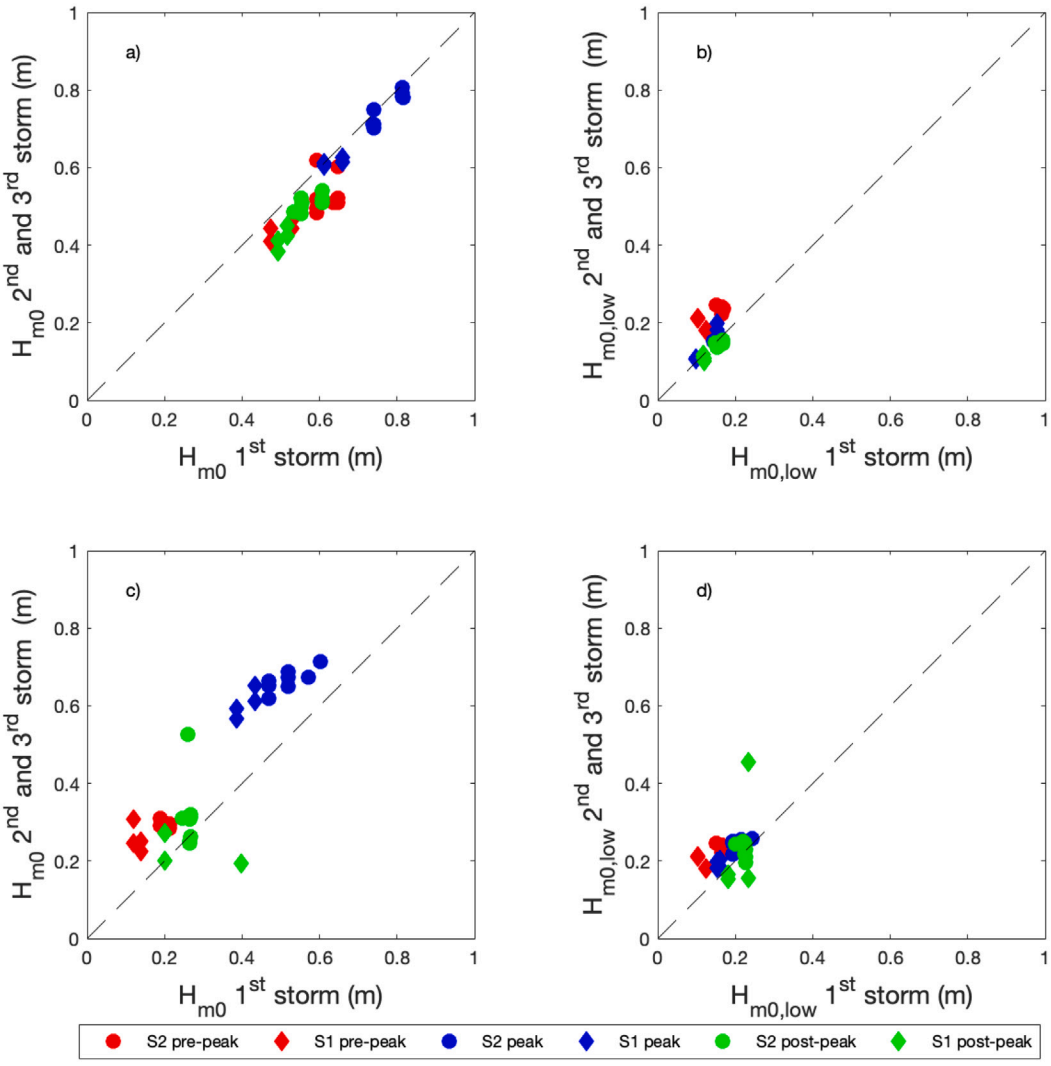

Fig. 10. H_{m0} and $H_{m0,low}$ for the first storm in a sequence versus the corresponding storm in different positions in the sequence. Circles S2, diamonds S1. (*a*) H_{m0} at the bar (WG 12) (*b*) $H_{m0,low}$ at the bar (WG 12). (*c*) H_{m0} at the toe of the structure (US 6 or PPS 8), (*d*) $H_{m0,low}$ at the toe of the structure (US 6 or PPS 8). (For interpretation of the references to colour in this figure legend, the reader is referred to the web version of this article.)

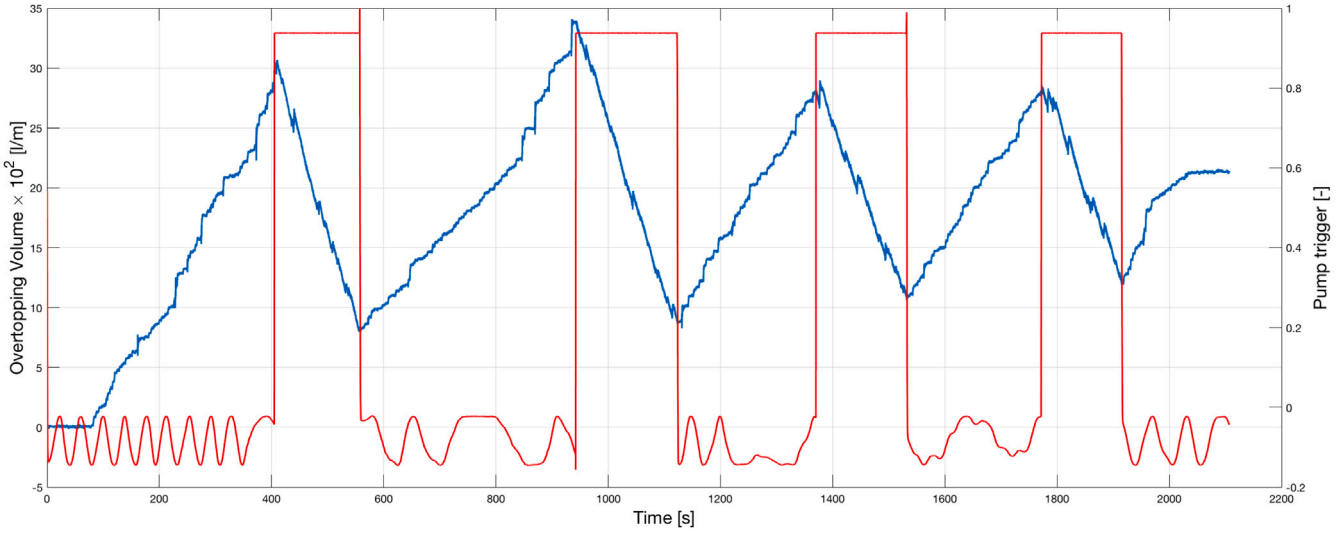

Fig. 11. Measured overtopping volume per unit length (blue line) and pump trigger (red line) for storm C1-1-S2-T4. (For interpretation of the references to colour in this figure legend, the reader is referred to the web version of this article.)

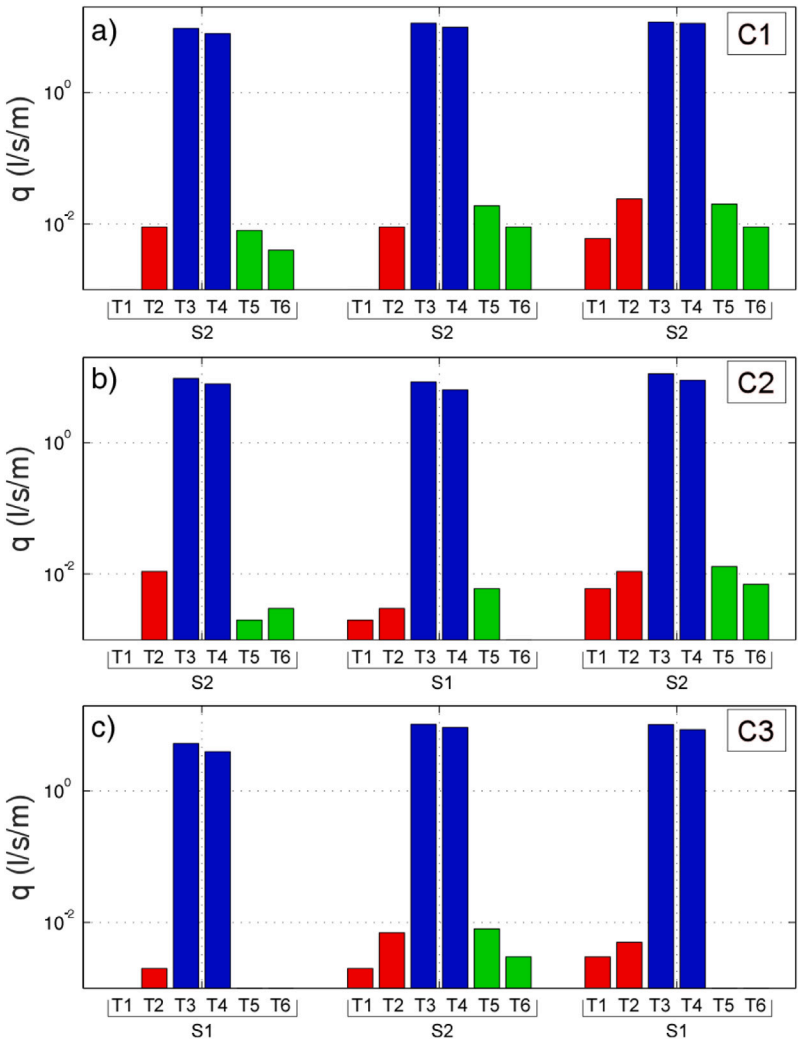

Fig. 12. q for all sequences. (*a*): C1, (*b*): C2, (*c*): C3. Red bars: pre-peak conditions (T1 and T2), blue bars: peak conditions (T3 and T4), green bars: post-peak conditions (T5 and T6). (For interpretation of the references to colour in this figure legend, the reader is referred to the web version of this article.)

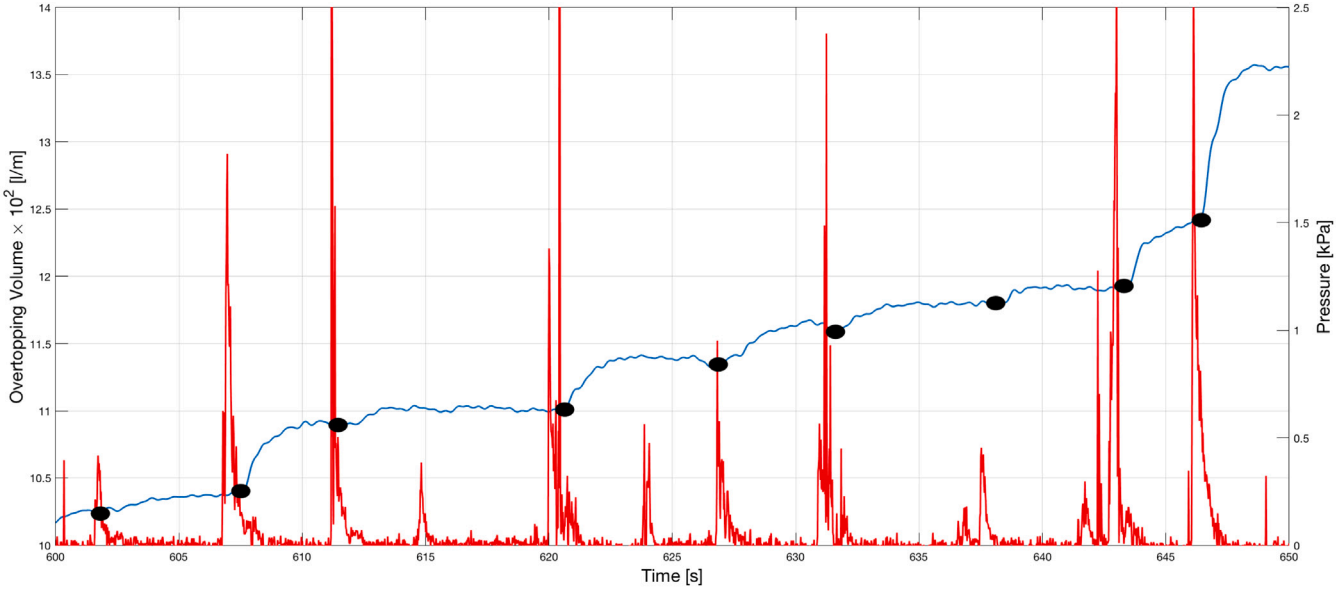

Fig. 13. Identification of overtopping events from the filtered signal of the cumulative overtopping volume per unit length (blue line) and PS 07 signal (red line) for storm C1-1-S2-T4. (For interpretation of the references to colour in this figure legend, the reader is referred to the web version of this article.)

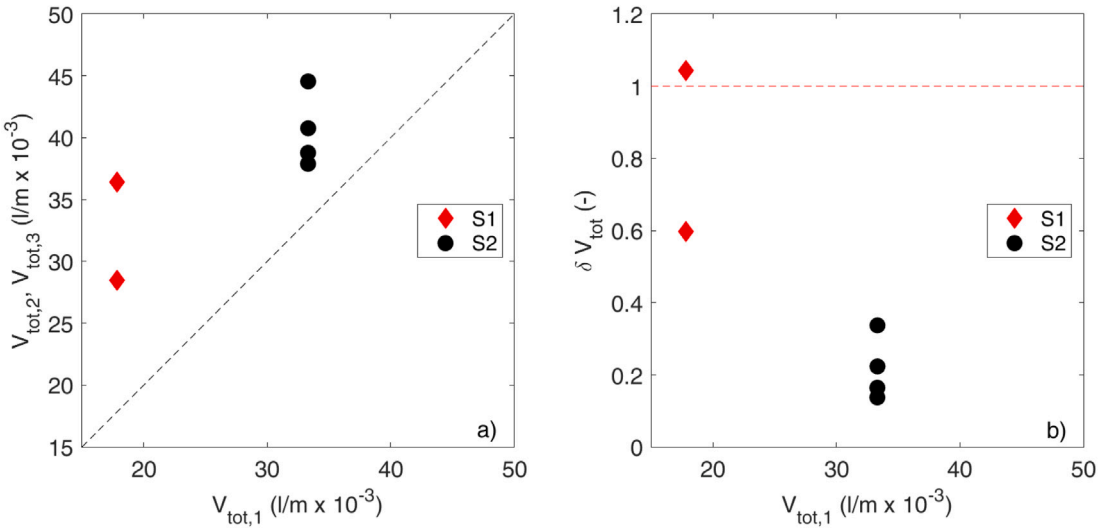

Fig. 14. (*a*) $V_{tot,2}$ and $V_{tot,3}$ versus $V_{tot,1}$ (*b*) δV_{tot} versus $V_{tot,1}$. Red diamonds: S1, Black circles: S2. (For interpretation of the references to colour in this figure legend, the reader is referred to the web version of this article.)

widely accepted for individual volumes (EurOtop, 2018) and it will be used here. The probability (P_v) that a certain overtopping volume V_i is larger than a value V is given by the two-parameter Weibull distribution:

$$P_v = P(V_i \geq V) = \exp\left[-\left(\frac{V}{a}\right)^b\right], \tag{1}$$

where b is a shape parameter and a is the scale parameter. A relationship between a and b is proposed in EurOtop (2018):

$$a = \frac{1}{\Gamma(1+b)\,\overline{V}}, \tag{2}$$

where $\overline{V}$ is the average overtopping volume, defined as the ratio between the total overtopping volume and the number of overtopping events in one sea state, and Γ indicates the Gamma function. As shown in EurOtop (2007) and EurOtop (2018), a small b value indicates that most overtopping events will have low volume, with only a few large ones. Conversely, a large b indicates that there will be more large overtopping volumes very similar in value. From the experiments, it is found that b increases with q for the same storm starting from different bed configurations, this positive correlation was also found in Zanuttigh et al. (2013). Also a follows a very similar behaviour. Fig. 15 shows two examples for selected sea states of C1 and C3 in order to highlight the influence of the position in the sequence on b. Using the classic Weibull plots, the empirical distribution of volumes are fitted to Eq. (1) to find b and a using Eq. (2). Panel a of Fig. 15 shows T3 for the three S2 in the sequence. b is determined by fitting the distribution to the largest volumes (e.g., $\ln(V/\overline{V}) > 0$, as done in Zanuttigh et al. (2013). This behaviour is consistent between the three repetition of S2 in C1 and the two S1 in C3, as panel b of Fig. 15 shows. The range of b found is 0.84–1.47. These values are higher than $b = 0.75$ found for vertical structures by Besley (1999), with most of them larger than $b = 0.85$ used in EurOtop (2018). Those measurements were probably made for limited overtopping discharge. With the very large overtopping the shape factor will increase, like for the smooth and rubble mound b in EurOtop (2018).

3.4.1. Role of the sequencing of storms on wave overtopping

Experimental results show that, for near-vertical structures at the back of a beach, there is an increase in wave overtopping volume for a storm that starts from an eroded barred beach configuration, rather than a simple slope. In the storm sequences tested this increase is larger for the less energetic storm in the sequence. When different stages of a storm are analysed, the increase is clearer for high water levels than

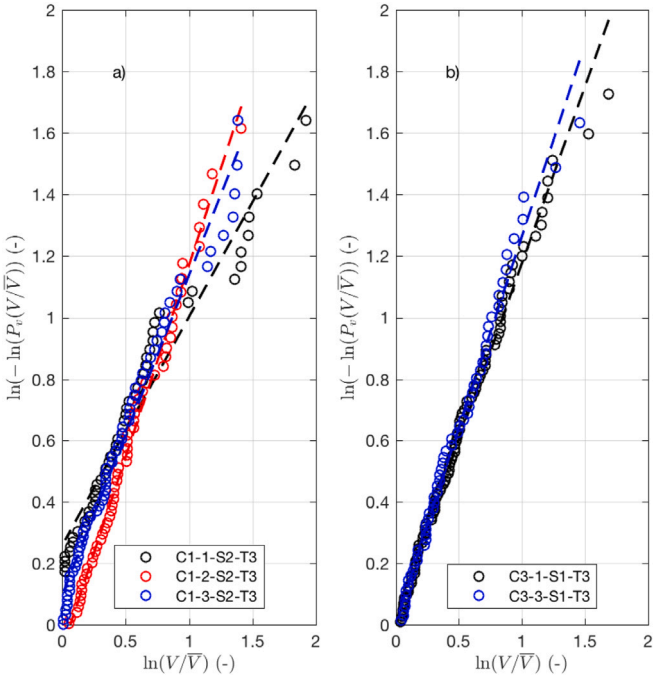

Fig. 15. Fitting of overtopping volume distributions on a Weibull chart. Circles: empirical probabilities, dashed lines: best fit. (*a*) Comparison between C1-1-S2-T3 (black), C1-1-S2-T3 (red), and C1-3-S2-T3 (blue). (*b*) Comparison between C3-1-S1-T3 (black) and C3-3-S1-T3 (blue). (For interpretation of the references to colour in this figure legend, the reader is referred to the web version of this article.)

in the lower levels. Wave conditions at the toe of the structure are always depth limited, hence the reason for the increase of the discharge is found in the evolution of the beach, in particular in Zones 3 and 4 identified in Fig. 6. Here erosion (i.e., scour) increases the significant wave height at the toe in the barred configuration with respect to the initial simple slope configuration. Indeed, in the presence of the seawall the material required to form the bar is claimed at the toe of the beach, where a significant scour occurs. At the same time the bar growth in Zone 2 produces an attenuation of the wave height due to breaking on the bar. Therefore, there are two competing processes that determine the wave height at the toe: one is enhanced dissipation induced by the bar, the other is increased water depth at the toe due to the erosion.

This latter appears to be dominant in these experiments when the same offshore incident wave conditions are compared. This mechanism also affects the distribution of overtopping volumes. These show that, when q increases for the same storm, due to the changed bed configuration, the average volume increases, as expected, and the range of volumes decreases, with a higher probability of large individual volumes of similar value. As a consequence, the impact of this behaviour on the level of safety from flooding is in apparent contrast with what found in natural beaches, where the presence of a bar mitigates the effect of the storms.

The comparison of V_{tot} between the two storms for different starting beach configuration (Fig. 14) summarises the findings of this work in terms of the effect of the sequence of storms. Overall, the behaviour of either storm S1 or S2 is qualitatively similar. In both cases the overtopping is less if the storm is the first of the sequence, i.e., the initial beach profile is linear, without a bar. Wave overtopping always increases after a preceding storm, however this is more evident for S1 than S2. In fact, whenever S1 occurs after S2, this produces nearly the same overtopping of the preceding S2. However, the influence of the initial conditions on overtopping decreased later in the sequence. This is due to the stabilisation of the bed configuration. As a consequence, previous storms may have less influence on the overtopping of subsequent ones, where the beach is closer to an equilibrium profile.

4. Conclusions

This work presents and discusses the results of a series of large-scale experiments on a near vertical 10/1 seawall and sandy foreshore, aimed at quantitatively investigating how wave overtopping is influenced by sequences of erosive storms. The experimental results allow to quantify the effect of the evolution of the 1/15 benchmark foreshore, due to sequences of erosive sea states, on wave overtopping. This is best shown by the change of V_{tot}, N_{ov}, and q among storms in each sequence. V_{tot} increases with the lowering of the beach in front of the seawall by up to 104%, due to the increase in H_{m0}. N_{ov} shows better the differences in overtopping for pre- and post-peak conditions. For example, in Table 5, it can be seen that N_{ov} for the T5 of the third S2 is three times N_{ov} of the first. For the same segment q increases by 2.5 times. A similar increase is shown also for the less energetic storm S1, however q is always of $O(10^{-3})$ l/s/m. Therefore, these results indicate that the lowering of the foreshore increases the level of overtopping, as expected. However, this increase is more evident in cumulative quantities like V_{tot} rather than in the overtopping rate because this stays within the same order of magnitude during peak conditions. Future overtopping assessment procedures might focus on this quantity to assess the flooding potential of a storm in a sequence. The laboratory investigation presented here relies on relatively low steepness wave conditions and idealised combination of SWL and incident wave characteristics, which represent limitations of the present study, together with scaling issues that are always present in mobile bed laboratory tests. Therefore, extensions to steeper conditions and, possibly, to field observation, are highly desirable. Nevertheless, the results on the quantification of the he role of the initial beach configuration on wave overtopping challenge existing predictive tools because of the role of initial beach profile is more evident from the total volume overtopped, rather than from the magnitude of the overtopping rate, prompting the need to give more relevance to cumulative quantities in wave overtopping prediction.

CRediT authorship contribution statement

Riccardo Briganti: Conceptualization, Methodology, Investigation, Data curation, Formal analysis, Writing – original draft, Writing – review & editing, Funding acquisition, Software, Supervision. **Rosaria Ester Musumeci:** Conceptualization, Methodology, Investigation, Data curation, Formal analysis, Writing – original draft, Writing – review & editing, Funding acquisition, Software, Supervision. **Jentsje van der Meer:** Conceptualization, Methodology, Investigation, Formal analysis, Writing – review & editing, Funding acquisition, Supervision. **Alessandro Romano:** Conceptualization, Methodology, Investigation, Data curation, Formal analysis, Writing – original draft, Writing – review & editing, Software, Visualisation. **Laura Maria Stancanelli:** Methodology, Investigation, Data curation, Formal analysis, Writing – original draft, Writing – review & editing, Software, Visualisation. **Matthias Kudella:** Investigation, Data curation, Resources, Supervision. **Rizki Akbar:** Investigation, Formal analysis. **Ryard Mukhdiar:** Investigation, Formal analysis. **Corrado Altomare:** Conceptualization, Investigation, Writing – review & editing. **Tomohiro Suzuki:** Conceptualization, Investigation, Writing – review & editing. **Paolo De Girolamo:** Conceptualization, Resources, Writing – review & editing. **Giovanni Besio:** Conceptualization, Methodology, Writing – review & editing. **Nicholas Dodd:** Conceptualization, Methodology, Supervision. **Fangfang Zhu:** Conceptualization, Investigation, Writing – review & editing. **Stefan Schimmels:** Conceptualization, Resources, Funding acquisition, Supervision.

Declaration of competing interest

The authors declare that they have no known competing financial interests or personal relationships that could have appeared to influence the work reported in this paper.

Acknowledgements

The work was supported by the European Union Horizon 2020 Research and Innovation Programme through the grant to HYDRALAB-PLUS, Contract no. 654110. We are grateful to all the staff in GWK for the hard work that made the experiments and analysis possible.

Appendix. Overtopping discharge computation

Two approaches were used to compute the mean overtopping discharge q for the experiments. The first used the information from the pump; the discharge pumped out was added to the discharge computed using the signal from the gravimetric tank, using the relationship:

$$q = \left(\frac{V_t(t = t_{end}) - V_t(t = t_0)}{W_c T_{test}} \right) + \left(\frac{\sum_{i=1}^{N_p} q_{p,i} T_{pump,i}}{W_c T_{test}} \right). \tag{A.1}$$

Here V_t is the volume of water in the tank, t is time, t_0 is the start time of the test and t_{end} the end time, $T_{test} = t_{end} - t_0$ is the actual test duration, W_c is the width of the chutes used in each test. For the pump, N_p is the number of times that the pump was used in a test, $q_{p,i}$ is the discharge of the pump in the i-th interval of usage, known from the pump calibration curve. $T_{pump,i}$ is the duration of the interval of usage. The second approach aimed to exclude any inaccuracy of the pump discharge from the measurement by computing q only over the time when the pump was not working:

$$q = \left(\frac{\sum_{i=1}^{N_q} \Delta V_{t,i}}{\sum_{i=1}^{N_q} T_{q,i}} \right) \frac{1}{W_c}, \tag{A.2}$$

where N_q is the number of intervals within the test in which the pump was not used, $\Delta V_{t,i}$ is the difference in volume of water in the tank for each interval, $T_{q,i}$ is the duration of each of these intervals.

Comparison between the results obtained using Eq. (A.1) with those obtained by Eq. (A.2), showed that the two methods used have a maximum percentage difference of 13.11% for C1-2-S2-T3. In two tests, (C2-1-S2-T3 and C2-1-S2-T4), only the initial part of the time series, in which the pumps were not used, could be used, as the tanks overflew during the tests even with pumping. This was due to the presence of two chutes and prompted the reduction to one chute only in subsequent high SWL tests. Given the small difference between the results of Eq. (A.1) and (A.2) and the fact that the latter was applicable to all cases, only the results obtained with Eq. (A.2) are used in this work.

Appendix B. Supplementary data

Supplementary material related to this article can be found online at https://doi.org/10.1016/j.oceaneng.2022.112024.

References

Akbar, R., 2017. The Influence of Foreshore Evolution during Storms on Wave Overtopping at a Steep Seawall – Large Scale Model Experiment. UNESCO-IHE Institute for Water Education, Delft, the Netherlands.

Altomare, C., Suzuki, T., Chen, X., Verwaest, T., Kortenhaus, A., 2016. Wave overtopping of sea dikes with very shallow foreshores. Coast. Eng. 116, 236–257.

Baldock, T.E., Gravois, U., Callaghan, D.P., Davies, G., Nichol, S., 2021. Methodology for estimating return intervals for storm demand and dune recession by clustered and non-clustered morphological events. Coast. Eng. 103924.

Besio, G., Briganti, R., Romano, A., Mentaschi, L., De Girolamo, P., 2017. Time clustering of wave storms in the Mediterranean sea. Nat. Hazards Earth Syst. Sci. 17 (3), 505–514.

Besley, P., 1999. Overtopping of Seawalls: Design and Assessment Manual. R&D Report W 178, Environment Agency, North East Region, p. 37.

Briganti, R., Musumeci, R.E., van der Meer, J.W., Romano, A., Stancanelli, L.M., Kudella, M., Akbar, R., Mukhdiar, R., Altomare, C., Suzuki, T., de Girolamo, P., Mancini, G., Besio, G., Dodd, N., Schimmels, S., 2018. Large scale tests on foreshore evolution during storm sequences and the performance of a nearly vertical structure. Coast. Eng. Proc. 36 (2018), papers.13.

Chen, X., Hofland, B., Uijttewaal, W., 2016. Maximum overtopping forces on a dike-mounted wall with a shallow foreshore. Coast. Eng. 116, 89–102.

Coco, G., Senechal, N., Rejas, A., Bryan, K.R., Capo, S., Parisot, J.P., Brown, J.A., MacMahan, J.H., 2014. Beach response to a sequence of extreme storms. Geomorphology 204, 493–501.

Dissanayake, P., Brown, J., Wisse, P., Karunarathna, H., 2015a. Comparison of storm cluster vs isolated event impacts on beach/dune morphodynamics. Estuar. Coast. Shelf Sci. 164, 301–312.

Dissanayake, P., Brown, J., Wisse, P., Karunarathna, H., 2015b. Effects of storm clustering on beach/dune evolution. Mar. Geol. 370, 63–75.

Eichentopf, S., Alsina, J.M., Christou, M., Kuriyama, Y., Karunarathna, H., 2020a. Storm sequencing and beach profile variability at Hasaki, Japan. Mar. Geol. 424, 106153.

Eichentopf, S., Karunarathna, H., Alsina, J.M., 2019. Morphodynamics of sandy beaches under the influence of storm sequences: Current research status and future needs. Water Sci. Eng. 12 (3), 221–234.

Eichentopf, S., Van der Zanden, J., Cáceres, I., Baldock, T.E., Alsina, J.M., 2020b. Influence of storm sequencing on breaker bar and shoreline evolution in large-scale experiments. Coast. Eng. 157, 103659.

EurOtop, 2007. EurOtop - Wave Overtopping of Sea Defences and Related Structures Assessment Manual. Pullen, T. and Allsop, N.W.H. and Bruce, T. and Kortenhaus, A. and Schüttrumpf, H. and van der Meer, J.W. Environment Agency, UK, URL http://www.overtopping-manual.com.

EurOtop, 2018. Manual on wave overtopping of sea defences and related structures. An overtopping manual largely based on European research, but for worldwide application. Van der Meer, J.W. and Allsop, N.W.H. and Bruce, T. and De Rouck, J. and Kortenhaus, A. and Pullen, T. and Schüttrumpf, H. and Troch, P. and Zanuttigh, B, http://www.overtopping-manual.com.

Franco, L., Geeraerts, J., Briganti, R., Willems, M., Bellotti, G., De Rouck, J., 2009. Prototype measurements and small-scale model tests of wave overtopping at shallow rubble-mound breakwaters: the ostia-rome yacht harbour case. Coastal Eng. 56 (2), 154–165.

Frostick, L.E., McLelland, S.J., Mercer, T.G., et al., 2011. Users guide to physical modelling and experimentation. IAHR Des. Manual.

Hofland, B., Chen, X., Altomare, C., Oosterlo, P., 2017. Prediction formula for the spectral wave period $T_{m-1,0}$ on mildly sloping shallow foreshores. Coast. Eng. 123, 21–28.

Kraus, N.C., McDougal, W.G., 1996. The effects of seawalls on the beach: Part I, an updated literature review. J. Coast. Res. 691–701.

Lee, G.-H., Nicholls, R.J., Birkemeier, W.A., 1998. Storm-driven variability of the beach-nearshore profile at duck, north Carolina, USA, 1981–1991. Mar. Geol. 148, 163–177.

Mansard, E.P., Funke, E., 1980. The measurement of incident and reflected spectra using a least squares method. Coast. Eng..

Masselink, G., Scott, T., Poate, T., Russell, P., Davidson, M., Conley, D., 2016. The extreme 2013/2014 winter storms: Hydrodynamic forcing and coastal response along the southwest coast of England. Earth Surface Proc. Landforms 41 (3), 378–391.

McDougal, W.G., Kraus, N.C., Ajiwibowo, H., 1996. The effects of seawalls on the beach: part II, numerical modeling of SUPERTANK seawall tests. J. Coast. Res. 702–713.

Mori, N., Suzuki, T., Kakuno, S., 2007. Noise of acoustic Doppler velocimeter data in bubbly flows. J. Eng. Mech. 133 (1), 122–125.

Mukhdiar, R.R., 2017. Nearshore Beach Evolution and Wave Overtopping by Large Scale Model Tests with Storm Clusters. UNESCO-IHE Institute for Water Education, Delft, the Netherlands.

Romano, A., Bellotti, G., Briganti, R., Franco, L., 2015. Uncertainties in the physical modelling of the wave overtopping over a rubble mound breakwater: The role of the seeding number and of the test duration. Coast. Eng. 103, 15–21.

Salauddin, M., Pearson, J.M., 2019. Wave overtopping and toe scouring at a plain vertical seawall with shingle foreshore: A physical model study. Ocean Eng. 171, 286–299.

Salauddin, M., Pearson, J.M., 2020. Laboratory investigation of overtopping at a sloping structure with permeable shingle foreshore. Ocean Eng. 197, 106866.

Sénéchal, N., Castelle, B., Bryan, K.R., 2017. Storm clustering and beach response. In: Coastal Storms. John Wiley & Sons, Ltd, pp. 151–174.

Splinter, K.D., Carley, J.T., Golshani, A., Tomlinson, R., 2014. A relationship to describe the cumulative impact of storm clusters on beach erosion. Coast. Eng. 83, 49–55.

Van Rijn, L.C., Tonnon, P., Sánchez-Arcilla, A., Cáceres, I., Grüne, J., 2011. Scaling laws for beach and dune erosion processes. Coast. Eng. 58 (7), 623–636.

Vousdoukas, M., Kirupakaramoorthy, T., Oumeraci, H., De La Torre, M., Wübbold, F., Wagner, B., Schimmels, S., 2014. The role of combined laser scanning and video techniques in monitoring wave-by-wave swash zone processes. Coast. Eng. 83, 150–165.

Williams, H.E., Briganti, R., Pullen, T., 2014. The role of offshore boundary conditions in the uncertainty of numerical prediction of wave overtopping using non-linear shallow water equations. Coast. Eng. 89, 30–44.

Williams, H.E., Briganti, R., Romano, A., Dodd, N., 2019. Experimental analysis of wave overtopping: A new small scale laboratory dataset for the assessment of uncertainty for smooth sloped and vertical coastal structures. J. Mar. Sci. Eng. 7 (7), 217.

Zanuttigh, B., van der Meer, J.W., Bruce, T., Hughes, S., 2013. Statistical characterisation of extreme overtopping wave volumes. Proc. ICE, Coasts Mar. Struct. Breakwaters.